


## Article

# Case Study from Máza Brickyard (SW-Hungary): Paleoecology and Sediment Accumulation Changes in the Southern Part of the Carpathian Basin

Dávid Molnár <sup>1,2,\*</sup> , László Makó <sup>3</sup>, Mihály Molnár <sup>4</sup> and Pál Sümegei <sup>1,2</sup>

<sup>1</sup> Department of Geology and Paleontology, University of Szeged, H-6722 Szeged, Hungary; sumegi@geo.u-szeged.hu

<sup>2</sup> Long Environmental Changes Research Team, Interdisciplinary Excellence Centre, Institute of Geography and Earth Sciences, University of Szeged, H-6722 Szeged, Hungary

<sup>3</sup> Institute of Plant Sciences and Environmental Protection, University of Szeged, H-6800 Hódmezővásárhely, Hungary; mako.laszlo@szte.hu

<sup>4</sup> INTERACT AMS Laboratory Nuclear Research Center, H-4026 Debrecen, Hungary; mmol@atomki.hu

\* Correspondence: molnard@geo.u-szeged.hu

**Abstract:** The loess–paleosol profile of Máza brickyard in SW Hungary was investigated through multivariate analyses of malacofauna and sedimentological analyses. The aim was to reconstruct the complex developmental history of both sediment and malacofauna. Three age–depth models were calculated, and the best-fit model, the OxCal P-sequence, was chosen for further analysis. The profile overlays the MIS3 and MIS2, beginning at approximately 45,000–50,000 cal BP and ending at the Pleistocene/Holocene boundary. The accumulation rates were two periods of intensive accumulation, equal to those observed in the Bácska Loess Plateau in Hungary, and two periods of decreased accumulation. Between ~38,000 and 31,000 cal BP, a decreased accumulation period was observed in Máza and other profiles from the Bácska Loess Plateau, indicating a common weak accumulation period at the end of MIS3. Correspondence and cluster analyses provided a higher-resolution paleoecological reconstruction, revealing a more detailed picture of the evolution of the studied section. The presence of thermophilous gastropod species with a high contribution to the correspondence analysis was significant in the sections. Although *Granaria frumentum*, *Helicopsis striata*, *Chondrula tridens*, and *Pupilla triplicata* were not significant species in the Máza malacofauna as a whole, their presence was associated with warming periods and the emergence of open vegetation.

**Keywords:** malacology; age–depth modelling; sediment accumulation; MIS2/MIS3; multi-variate statistics; loess–paleosol sections



**Citation:** Molnár, D.; Makó, L.; Molnár, M.; Sümegei, P. Case Study from Máza Brickyard (SW-Hungary): Paleoecology and Sediment Accumulation Changes in the Southern Part of the Carpathian Basin. *Quaternary* **2024**, *7*, 35. <https://doi.org/10.3390/quat7030035>

Academic Editor: James B. Innes

Received: 28 May 2024

Revised: 28 June 2024

Accepted: 12 August 2024

Published: 15 August 2024



**Copyright:** © 2024 by the authors. Licensee MDPI, Basel, Switzerland. This article is an open access article distributed under the terms and conditions of the Creative Commons Attribution (CC BY) license (<https://creativecommons.org/licenses/by/4.0/>).

## 1. Introduction

The significance of loess and loess-like sediments as terrestrial alternatives to marine and ice-core drilling has been widely recognized for several decades [1]. Since then, extensive research has been conducted in various loess-covered regions around the world to provide researchers with a more accurate paleoenvironmental reconstruction of the study area and to compare these results with those from marine and ice-core drillings. A number of multi-proxy studies have been published globally [2–8], but it should be noted that the investigation methods used in these studies vary widely. A similar situation exists in European loess investigations, including those in the Carpathian Basin. The applied methods can be broadly classified into two categories: sedimentary and paleoecological. Additionally, there are also research groups that use “hybrid” methods, which combine sedimentary methods with paleoecological (mainly malacological) methods, e.g., [9–12]. The Carpathian Basin loess research is also characterized by a similar dichotomy, with pure sedimentary studies also occurring here (e.g., [13–17]) alongside the paleoecological

(e.g., [18–21]) and “hybrid” studies (e.g., [21–29]). The research on the Carpathian Basin loess–paleosol sections holds great significance, as there is no evidence of a persistent ice sheet in the area during the Pleistocene [22]. Furthermore, recent studies have revealed that the basin lies within two loess domains [30] (Figure 1). Additionally, the basin possesses unique climatic and environmental conditions [22], which are reflected in the specific characteristics of each site.

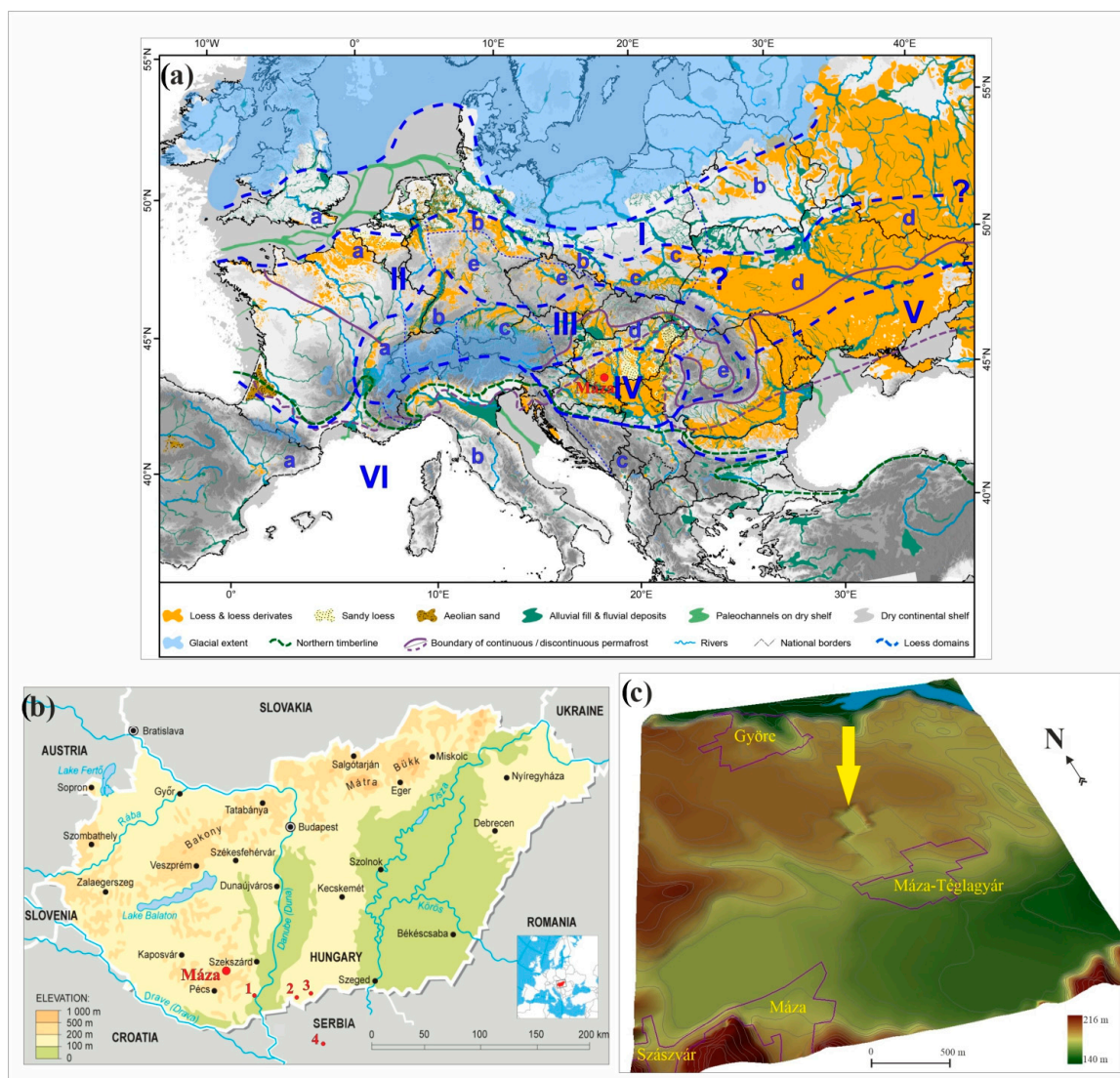


**Figure 1.** Location of the loess–paleosol profile of Máza brickyard (a) in the European loess area (M) [30], (b) in Hungary, and (c) a 3D digital topographic model of its close vicinity (yellow arrow shows the exact location of the profile; other mentioned loess–paleosol sequences in the text: 1 Dunaszekcső, 2 Katymár, 3 Madaras, 4 Črvenka).

In our current study, we have supplemented the previously published malacological findings from the Máza brickyard loess–paleosol section [21] with age–depth models based on radiocarbon age data and sedimentological results, including environmental magnetism, grain size distribution, and organic matter/carbonate content. Moreover, we have reinterpreted the previously published dominance-based malacological results from different viewpoints and performed multivariate statistical analyses to better understand the faunal variations. By comparing the results with the age–depth models, we have achieved a high-resolution temporal interpretation of the sedimentary geological and paleoecological data, as well as an exploration of the loess accumulation phases.

### *List of Abbreviations in the Text*

a.s.l.—above sea level; cal BP yr—calibrated year before present; AMS—accelerator mass spectrometry; AR—accumulation rate; CI—confidence interval; MAR—mass accumulation rate;  $\rho_{1,2}$ —bulk densities; SR—sedimentation rate;  $f_{eol}$ —mass concentration of aeolian materials; GSI—grain size index;  $\chi_{LF}$ —low-frequency mass specific magnetic susceptibility;  $\chi_{FD}\%$ —frequency-dependent magnetic susceptibility; LOI—loss on ignition; PCA—principal component analysis; CA—correspondence analysis; MZ—malacological zone; CL—cluster; LGM—last glacial maximum; MIS—marine isotope stages; GI—Greenland interstadial; GS—Greenland stadial; and NGRIP—North Greenland Ice Core Project.

## **2. Study Site and Lithology**

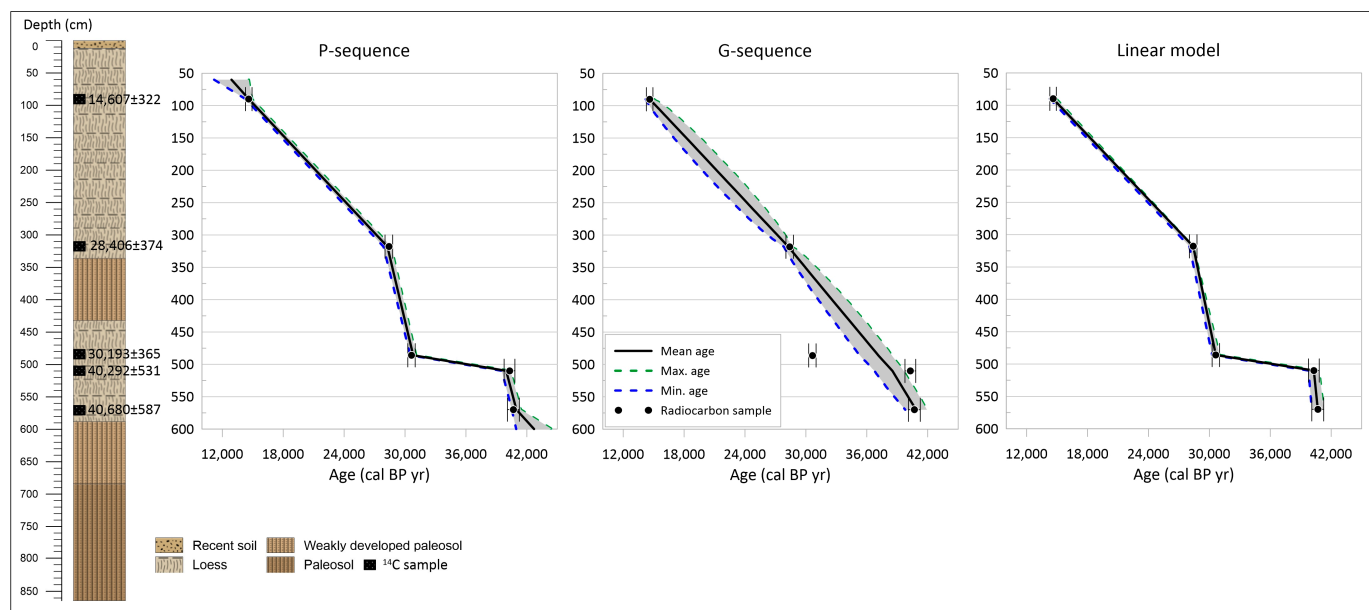
The area under investigation is located in southwest Hungary, specifically in the northern foothills of the Mecsek Mountains on a plateau that gently slopes down to the north. It falls within the fourth loess domain of Europe [30] (Figure 1). The surrounding region, known as Völgység, translates to “valley land” due to its position between the Mecsek Mountains and the Szekszárd Hills [31]. The Máza sequence can be found between the villages of Máza and Nagymányok in the northern part of the former mining area of an old brick factory (46°17′09.58″ N, 18°24′21.15″ E) at an elevation of 164 m above sea level. The height of the south-facing profile is 864 cm [21].

Figure 1 depicts three additional loess–paleosol sections in addition to the Máza section: Dunaszekcső (1), Katymár (2), and Madaras (3), all situated in Hungary, and Črvenka (4) in Serbia. The Dunaszekcső section is situated on the high right bank of the Danube River. The remaining three loess–paleosol sections are located on the Bácska-Titel loess plateau and were formed during a similar period, the Late Pleistocene and radiocarbon age data from all sections were accessible for running age–depth models. The Dunaszekcső section, which was investigated through multi-proxy analyses [32–34], reveals a section of more than 18 m in thickness that was eroded by the Danube River. Approximately 120 radiocarbon age data, spanning ca. 40,000–23,000 cal BP yr [34], are available from this section. The Katymár brickyard section [35] is a 10.32 m high wall in an abandoned brickyard site, from which nine radiocarbon ages were obtained, ranging from about 39,000 to 15,000 cal BP yr (approximately 50–1050 cm). The Madaras brickyard section [26], constructed on the wall of an abandoned brickyard, stands at a height of 10 m, and 19 radiocarbon dates, covering the time interval between about 39,000 and 12,000 cal BP yr (about 20–1000 cm), are available. The Črvenka section [25,36] is also located in the wall of a brickyard and has a height of 12 m, with six radiocarbon age data available for the age–depth models, covering the interval between 40,000 and 7000 cal BP yr (approximately 50–600 cm).

## **3. Materials and Methods**

### *3.1. Sampling and Lithology*

The profile was divided into six lithological layers, consisting of two loess layers and four paleosol layers (Figure 2) [21]. Samples were collected at a 12 cm interval from the Máza brickyard, resulting in a total of 72 samples.



**Figure 2.** Lithologic description with radiocarbon ages, and the calculated age–depth models based on the radiocarbon data of Máza brickyard.

### 3.2. Age–Depth Modelling and Accumulation Intensity

In the AMS radiocarbon dating process, snail shells were cleaned using ultrasonic washing to remove surface contaminants as well as carbonates. Then, 2% hydrochloric acid was used to etch the shells, which resulted in ca. 20–30% material weight reduction. After drying, the acid-cleaned shells were placed in vacuum-tight two-finger reaction ampoules (with an inner volume of approximately 100 cm<sup>3</sup>) and dissolved by phosphoric acid (85% aq). The resulting CO<sub>2</sub> was purified cryogenically and then graphitized [37,38]. The <sup>14</sup>C measurements were conducted using MIDCAS (compact radiocarbon AMS system), which was developed at the Paul Scherrer Institute and ETH Zürich [39,40]. This system was installed at the Hertelendi Laboratory of Environmental Studies, Debrecen, in 2011 [38]. Five AMS radiocarbon measurements were available for modeling, one from the DirectAMS Lab, Seattle, WA, USA, and four from the ICER Lab, Debrecen, Hungary. All radiocarbon measurements were obtained from snail shells (Table 1).

**Table 1.** Calibrated and uncalibrated radiocarbon data from Máza brickyard, based on *Trochulus hispidus* shells.

Depth (cm)	Material	BP yr	+/-	Calibrated Age Range Min	Calibrated Age Range Max	Mean Age (cal BP yr)	+/-	Lab Code	Probability Distribution	Used for Age Model
90	shell	12,432	49	14,285	14,930	14,607	322	DeA-20934	100%	yes
318	shell	24,278	123	28,032	28,780	28,406	374	DeA-20935	100%	yes
414	shell	19,361	98	23,026	23,450	23,238	212	D-AMS 002121	69.3%	no
486	shell	26,379	148	30,273	31,003	30,638	365	DeA-20936	100%	yes
510	shell	35,156	224	39,761	40,823	40,292	531	D-AMS 002122	100%	yes
570	shell	35,632	292	40,093	41,267	40,680	587	DeA-20937	100%	yes

Given the distinct pedogenetic processes and compaction that occur during loess layer deposition [41], it is probable that the actual sedimentation rate fluctuated, resulting in varying temporal resolutions for each layer in our study profile [42]. To address this, we utilized several types of age–depth models for our dataset. One of the models we employed



was the classical model of linear interpolation [43], which has been used in earlier research. This model assumes that accumulation rates were constant between neighboring dated depths and abruptly changed at the exact dated depths [44,45].

In this research, the Bayesian modeling was executed by employing Poisson and gamma distributions as initial data for accumulation rates. The Bacon model [46] utilizes an autoregressive process with gamma innovations to model accumulation rates for numerous uniformly spaced depth segments. The inverse accumulation rates (expressed as year/cm) were estimated from 27.06 million Markov Chain Monte Carlo (MCMC) iterations, which were then utilized to construct the age–depth model. The accumulation rate (AR) model was initially constrained by default prior information, including an accumulation shape of 1.5 and an accumulation mean of 20 for the beta distribution, a memory mean of 0.7, and a memory strength of 4 for the beta distribution, which describes the autocorrelation of the inverse AR (Supplementary Figure S1). All input data were given in 14C yr BP, and the model used the northern hemisphere IntCal20 calibration curve [47] to convert conventional radiocarbon ages to calendar ages expressed as cal BP. The age modeling was run initially to achieve a final resolution of 12 cm. The fit of the posterior gamma and beta distributions, as well as the 95% CI ranges, and the inverse accumulation rate (AR) with 95% CI ranges, were considered while comparing models. Ultimately, age–depth modeling was carried out using the set parameters. All data and figures are presented in calendar ages expressed as cal BP.

The P-sequence of OxCal modeling [48] was utilized with a size-dependent granularity (silt) ( $k = 0.3$ ) of the predominant grain in the sequence by conducting 3.989 million iterations. Furthermore, to evaluate sensitivity, the granularity ( $k$ ) was modified to account for variable rates of sedimentation. The P-sequence calculated ages for 1-cm intervals with 95% confidence intervals to determine the uncertainty of the model. The estimates were calculated from the mean values. The results obtained from the OxCal and Bacon models were examined for consistency, integrity, and statistical significance. Additionally, the mean 95% confidence ranges, as well as the maximum and minimum confidence values, were computed and compared to evaluate the precision of the ages for different parts of the profile. These approaches enabled the assessment of the chronological sharpness of the models [49].

By determining the sedimentation rate, the mass accumulation rate could be calculated. The mass accumulation rate (MAR in  $\text{g}/\text{cm}^2/\text{ky}$ ) represents the amount of loess accumulated at a specific location [50]. Initially, the absolute sedimentation rate per unit (SR in  $\text{cm}/\text{year}$ ) was estimated. The loess-related bulk density values were calculated using global (bulk density 1) [51,52] and Hungarian results (bulk density 2) [13]. In the evaluation, bulk density 2 was employed as it is the most appropriate estimate given the regional properties of the loess. The use of the same values by others will facilitate correlations [24,32,35].

### 3.3. Sedimentological Analyses

The grain size composition of sedimentological samples was determined using the laser particle sizing method [53]. Following the treatment of the dried samples with 30% hydrogen-peroxide and 10% hydrochloric acid to eliminate organic matter and carbonates, the samples were transferred to a 5% solution of sodium hexametaphosphate to prevent particle agglomeration. The OMEC EasySizer 20 laser diffraction particle sizer was utilized to measure the samples for 42 intervals ranging from 0.0001 to 0.5 mm at the Department of Geology and Paleontology, Szeged University, Hungary. The EasySizer 20 employs Mie's scattering theory, with the carrier medium being water (refractive index 1.333) and the sediment possessing a uniform refractive index of 1.544 (quartz 1.545; illite 1.575; orthoclase 1.53; anorthoclase 1.525). The cumulated percentage ratio was calculated for each grain size range in accordance with Wentworth's scale. The U-ratio ( $16\text{--}44\ \mu\text{m}/5.5\text{--}16\ \mu\text{m}$ ) was calculated to determine the dominant and subordinate phases of wind transport during cold–warm and dry–wet periods [52–56]. High U-ratio values indicate more intense sedi-

ment transport, which is characteristic of dry periods, while low values may suggest wet periods. Additionally, the grain size index (GSI—20–50  $\mu\text{m}$ / $<20 \mu\text{m}$ ) was calculated, which considers the clay fraction and is suitable for determining the formation, transportation, and accumulation of loess [57,58]. The GSI, like the U-ratio, is a measure of climatic conditions during sediment accumulation, but post-accumulation processes such as pedogenesis also play a role. Low GSI values indicate a wet climate or soil formation, while high GSI values indicate dry climatic conditions.

Environmental magnetic analyses were conducted on bulk samples [59–63]. Initially, the samples were weighed and crushed in a glass mortar. Subsequently, the samples were placed in plastic boxes and dried in an oven at 40 °C for 24 h. Next, the low (0.465 kHz— $\kappa_{\text{LF}}$ ) and high-frequency (4.65 kHz— $\kappa_{\text{LF}}$ ) magnetic susceptibilities were measured using an MS2 Bartington magnetic susceptibility meter equipped with an MS2B dual frequency sensor [64] in the Department of Geology and Paleontology, Szeged University, Hungary. The  $\kappa$  values were utilized to calculate the mass-specific ( $\chi_{\text{LF}}$ ) and frequency-dependent ( $\chi_{\text{FD}}\%$ ) magnetic susceptibilities [64]. All samples were measured three times, and the average values of magnetic susceptibility were computed and reported.

The determination of changes in organic matter and carbonate content loss on ignition (LOI) was carried out [65,66]. The samples were heated in a programmable electric furnace at 550 °C and 900 °C for 1–1 h, during which the organic matter and then the carbonate content were burnt out of the samples. The mass loss was measured after each combustion. The results are presented in percentage distribution.

### 3.4. Malacology

The procedures for collecting, cleaning, and identifying malacological samples were carried out according to the methods outlined by Endre Krolopp and Pál Sümegei [22,67,68]. At Máza brickyard, approximately 5 kg of bulk samples were collected from every 12 cm interval of the sequence, resulting in a total of 72 mollusk-bearing samples. The sediment was then washed through sieves with a mesh size of 0.8 mm, dried, and the identifiable shells and fragments were sorted and identified. The identification of these samples, as well as knowledge of each species' climatic and environmental demands, is essential for creating paleoecological reconstruction datasets [67,69–71]. This modern knowledge is applied to interpret paleoenvironmental changes from fossil data, including absolute and relative abundance diagrams of species and ecological groups, by utilizing the principle of actualism [10,12,67]. The ecology of each species is well understood based on modern samplings, and species have been classified into ecological groups that may differ from one region to another, based on species temperature, humidity, and vegetation preferences [9,22,61,68,71–73]. All three factors are interdependent, and even changes in other, less important conditions can affect them.

In addition to the dominance and abundance analyses, more sophisticated statistical analyses were also conducted. The diversity of a community, including the malacofauna, can be well characterized by the Shannon index  $H'$  [74], which is calculated as follows:

$$H' = -\sum_{k=1}^n p_k \ln p_k$$

where  $n$  equals the number of species and  $p_k$  the frequency of the  $k$  species ( $k$  varying between 1 and  $n$ ).

Principal component analysis (PCA) was employed to analyze the malacological data table [75], which included assemblages in the columns and species' real abundance values in the rows. The correlation matrix was utilized for the analysis. The loadings for the 1st principal component provided an estimate of temperature variation, while the loadings for the 2nd principal component were used to estimate the wet/dry environmental conditions [76].

Correspondence analysis (CA) [77] is a valuable method for examining the distribution and importance of malacological data, particularly the distribution and importance of snail

species found on the site. It can also provide a good estimation of the role of temperature and humidity on the snail fauna in the studied section [9,73,76,78–80]. Before conducting the CA analysis, the abundance values of the malacological data table were converted using a logarithmic method to avoid large variations in abundance [78], which is referred to as “Rousseau-coding” (Supplementary Table S1). The resulting data table was used for the CA calculation, where the total abundance was 1510. The data were used to produce a scatter plot showing the distribution of snail species along the X and Y axes. Further calculations are necessary to determine the importance of species [9,77,80]. Utilizing the data table in Supplementary Table S1, we calculate the mass of each species. By multiplying the masses by the square of the axis values for the species, we obtain the contribution of inertia of the axes. Multiplying the inertia values for each species by the eigenvalue of the corresponding axis (total inertia) gives the contribution of each species.

Cluster analysis was utilized for zonation calculations in the malacological domain. Ward’s method [81] was employed on the logarithmic data table for the analysis. For diversity counts and multivariate statistical analyses, including cluster analysis, PCA, and CA, the Past 4.16 software kit [82] was utilized.

#### 4. Results

In the field, the lithologic description of the Máza section was conducted, revealing that the uppermost 12 cm of the profile comprised recent soil. Between 12 and 336 cm, a homogenous loess layer was deposited, containing significant mollusk shells and carbonate content. A weakly developed paleosol layer with increased organic matter and clay content was situated between 336 and 432 cm. From 432 to 588 cm, a second loess layer was deposited with high carbonate and moderate snail shell content. Another weakly developed paleosol layer was located between 588 and 684 cm, exhibiting increasing clay and organic matter content. This trend continued in the lowermost paleosol layer, which developed between 684 and 864 cm. Regrettably, the bottom of this layer has not been uncovered.

##### 4.1. Age–Depth Modelling and Accumulation Intensity

Previous and recent research has demonstrated that utilizing a single age–depth model may not result in the most accurate modeling. Therefore, it is recommended to employ at least two or more models to identify the most suitable one [26,28]. For the loess/paleosol profile of Máza brickyard, three different age–depth models were calculated: OxCal’s P-sequence, Bacon’s G-sequence, and the classical linear model, taking into account only the available radiocarbon ages (Figure 2). The accumulation rates (AR) were calculated from every sequence (Figure 3). All of the calculated sequences overlap the loess–paleosol profile between 90 and 600 cm, spanning approximately 13,000–43,000 cal BP yr.

The P-sequence and linear sequence exhibit similarities in their graphs, as they accurately reflect the placement of radiocarbon dates on the chart. In contrast, the G-sequence appears to be more linear and exhibits a higher deviation in its minimum and maximum ages compared to the other two. This discrepancy can be attributed to the different calculation methods employed by OxCal and Bacon, with Bacon’s G-sequence modeling a relatively linear shape and low deviation of counted values [83,84]. Despite this similarity, the P-sequence is considered to be the most accurate and applicable model, as it is derived from a cm resolution age calculation, while the linear sequence utilizes only five radiocarbon ages.

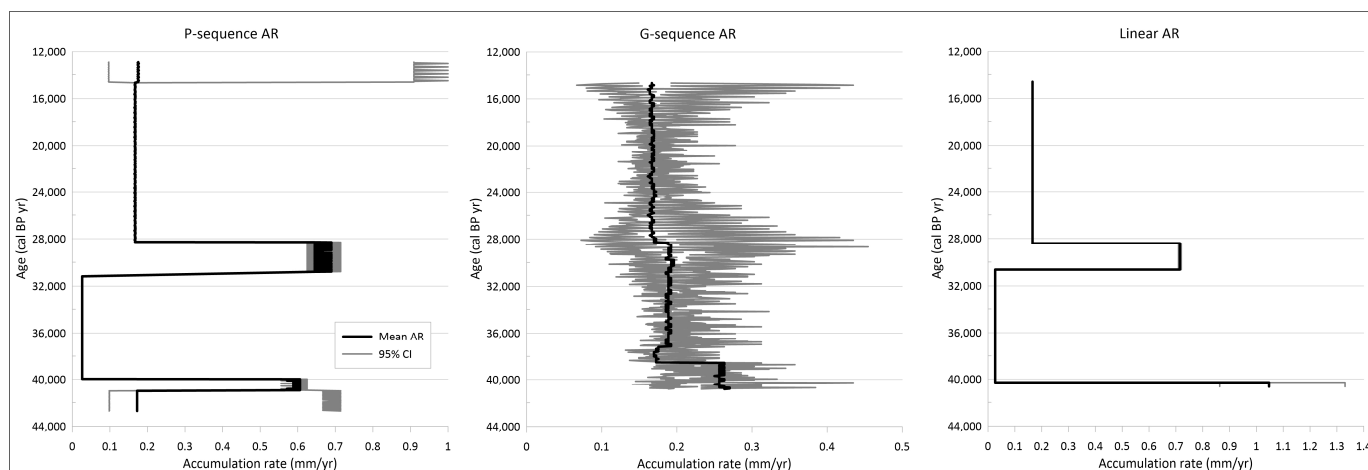


**Figure 3.** The calculated accumulation rate (AR) of each age–depth model of Máza brickyard.

Upon examining the P-sequence, a break can be observed around 30,000–40,000 cal BP, resulting in the lowest AR values of the P-sequence (Figure 3). A comparison of the AR charts reveals significant differences between the sequences, with the P- and linear sequence exhibiting fluctuating accumulation intensities and low 95% confidence intervals (CI), while the G-sequence displays a roughly linear accumulation with meaningful CI values. These differences are also reflected in the AR charts, which were calculated from the age–depth models. According to the AR chart of the P-sequence, the accumulation intensity can be divided into four periods (Figure 3).

During a period spanning approximately 42,700 to 41,500 cal BP yr, the accumulation rate (AR) values were around 0.18 mm/yr. Subsequently, the values increased to approximately 0.6 mm/yr between 41,500 and 40,000 cal BP yr, which were higher than the values of the G-sequence (0.25 mm/yr) but lower than the linear sequence (approximately 1.1 mm/yr). The linear AR values were around 1.05 mm/yr during this period. Between approximately 40,000 and 31,000 cal BP yr, the AR values decreased to around 0.03 mm/yr, which may have been due to the dry climate resulting in an erosional horizon. The next period lasted from approximately 31,500 cal BP yr to approximately 28,000 cal BP yr, during which the highest AR values were recorded. The mean values were around 0.65 mm/yr, with CI values fluctuating between 0.6 and 0.75 mm/yr. The increased accumulation may have indicated more humid weather with reduced sediment particle mobility and/or denser vegetation cover, where the vegetation cover protects the particles from wind erosion. This period coincides with the formation of the upper weakly developed paleosol, suggesting that the high AR values may have been indicative of warmer and more humid climatic conditions. The fourth period lasted from approximately 28,000 cal BP yr to approximately 12,700 cal BP yr, during which the AR decreased to around 0.2 mm/yr, with CI values fluctuating between approximately 0.1 and 0.3 mm/yr.

When comparing the results of Accumulation Rates (AR) with Mass Accumulation Rates (MAR), it can be observed that the values for the four periods generally followed the trend of AR (Figure 3; Table 2). The MAR values were computed using linear ages, and thus, the best-fit model for the MAR values would be a linear sequence. However, the higher accumulation periods (around 41,500 to 40,000 and approximately 31,500 to 28,000 cal BP yr) yielded high MAR values of 2320 g per square meter per thousand years ( $\text{g}/\text{m}^2 \times \text{ky}$ ) for the older period and 1410  $\text{g}/\text{m}^2 \times \text{ky}$  for the younger accumulation peak (Table 2).



**Table 2.** The calculated mass accumulation rates (MAR) from Máza brickyard with bulk densities 1 and 2 ( $\rho_1$  and  $\rho_2$ ); SR represents the sedimentation rate and  $f_{eol}$  means the mass concentration of aeolian materials.

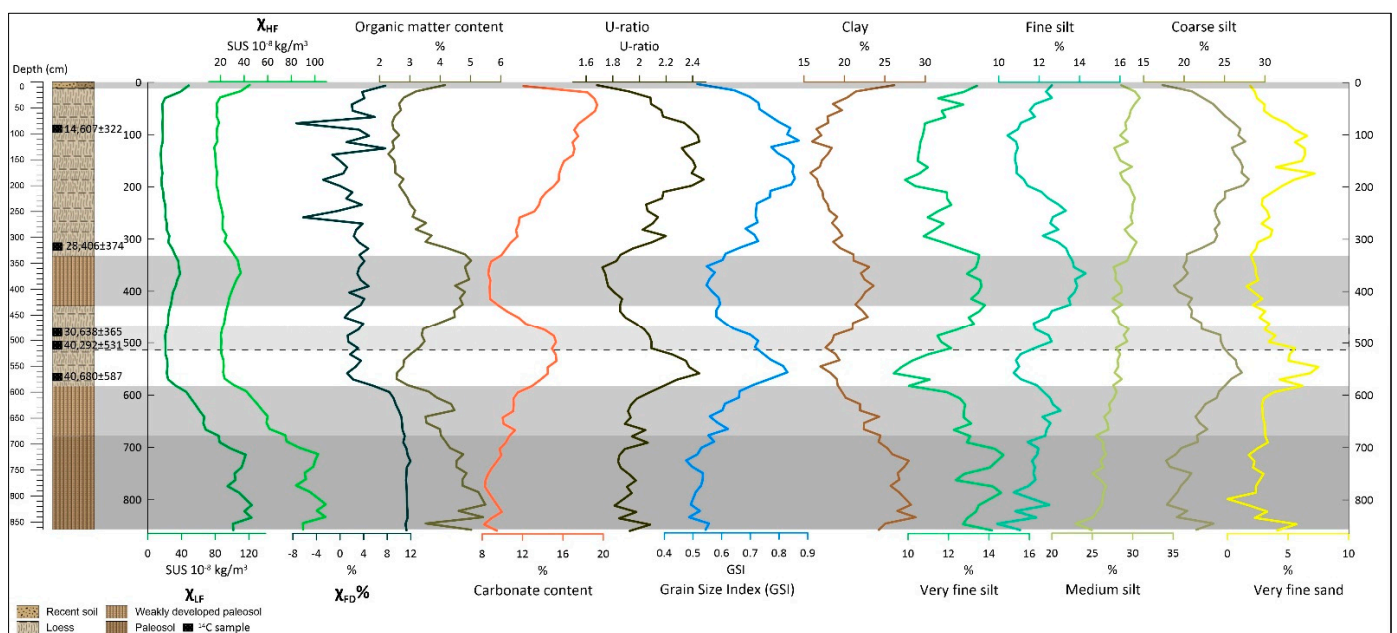
Age (cal. BP)	Depth (cm)	MAR (Bulk Density 1)		$f_{eol}$	MAR ( $\text{g/m}^2 \times \text{ky}$ )
		SR (cm/Year)	$\rho_1$ ( $\text{g/cm}^3$ )		
14,607	90	0.016523	1.6	1	264
28,406	318	0.094012	1.65	1	1551
30,193	486	0.002376	1.65	1	39
40,292	510	0.154639	1.65	1	2552
40,680	570	-	-	Mean:	1102

Age (cal. BP)	Depth (cm)	MAR (bulk density 2)		$f_{eol}$	MAR ( $\text{g/m}^2 \times \text{ky}$ )
		SR (cm/Year)	$\rho_2$ ( $\text{g/cm}^3$ )		
14,607	90	0.016523	1.5	1	248
28,406	318	0.094012	1.5	1	1410
30,193	486	0.002376	1.5	1	36
40,292	510	0.154639	1.5	1	2320
40,680	570	-	-	Mean:	1003

#### 4.2. Sedimentological Analyses

The sedimentological analyses of the 72 samples taken from the Máza loess–paleosol profile revealed six sedimentological layers, as indicated by the results and lithology (Figure 4). The lowest layer overlaps the paleosol between 864 and 684 cm and is characterized by the highest magnetic susceptibility ( $\chi_{LF}$ ) values, which vary between 80 and  $120 \times 10^{-8} \text{ kg/m}^3$ . Additionally, the organic matter content is significantly high (~5%) in this layer, and the  $\chi_{FD}\%$  values are also the highest (~12%) in this layer. The clay content has the highest ratio, approximately 25%, besides the 45% coarse and medium silt ratio. Moreover, a constant ~3% of very fine sand could be observed, and the U-ratio and grain size index (GSI) values are consistently low in this layer.



**Figure 4.** Results of the sedimentological analyses from Máza brickyard (the dashed horizon represents the later discussed main sedimentological contradiction of the section).

The second layer (684–588 cm) can be described as the lower weakly developed paleosol layer. The  $\chi_{LF}$  values gradually decreased to  $90 \times 10^{-8} \text{ kg/m}^3$  and then  $35 \times 10^{-8} \text{ kg/m}^3$  upwards. The  $\chi_{FD}\%$  remained at approximately 12% and only decreased in the uppermost part. The clay content decreased by about 20%, and the sand content was still around 5% in this layer. The ratio of coarse and medium silt increased slightly, approximately 50% of the grain-size distribution. The organic matter content decreased, while the carbonate content slightly increased.

The third layer in the sequence overlaps the lower loess layer, spanning a depth of 588–432 cm (corresponding to approximately 42,010–29,990 cal BP yr). The average  $\chi_{LF}$  values were around  $20\text{--}30 \times 10^{-8} \text{ kg/m}^3$  throughout the entire layer, while the  $\chi_{FD}\%$  fluctuated between 0 and 4%. The clay content decreased to roughly 17% at 550 cm before beginning to rise again, reaching a ratio of 21–22% at 432 cm. The sand ratio also increased, with several samples exhibiting more than 5% of sand content. A peak in the U-ratio and GSI graphs is observed at around 550 cm, and the carbonate content shows high values of around 14–16% in this region.

The next layer in the sequence overlaps the upper weakly developed paleosol layer, which ranges from 432 to 336 cm (corresponding to approximately 29,900–28,500 cal BP yr). In this layer, the  $\chi_{LF}$  values exhibit a slight protrusion, with maximum values of around  $40 \times 10^{-8} \text{ kg/m}^3$ . The  $\chi_{FD}\%$  values are relatively stable, hovering around 4%. The organic matter content increases to around 5%, while the clay content rises slightly to approximately 23%. The sand content, on the other hand, decreases to around 3%.

The fifth layer is the upper loess layer, spanning a depth of 336–12 cm (corresponding to approximately 28,500 to 11,000 cal BP yr). In this layer, the  $\chi_{LF}$  values decrease overall, averaging around  $20 \times 10^{-8} \text{ kg/m}^3$ . However, the  $\chi_{FD}\%$  values show significant fluctuations, with a maximum peak of around 140 cm. The clay content falls below 20%, while the sand content increases to around 7–8%. The ratio of coarse and medium silt remains approximately 75%. The carbonate content exhibits the highest values, reaching around 15–60 cm with approximately 18% of the content.

The uppermost layer is characterized by significant changes in the sedimentological results. The  $\chi_{LF}$  values rapidly increase to approximately  $40 \times 10^{-8} \text{ kg/m}^3$ , starting to rise even in the fifth layer. The  $\chi_{FD}\%$  values also increase to around 8%. The clay content rises to approximately 25%, while the ratio of coarse and medium silt decreases to around 45%. The organic matter content continues to increase as well.

#### 4.3. Malacology

The results of previous studies [21] and recent malacological findings indicate that the malacofauna has undergone significant changes (Supplementary Figure S2). The multivariate analysis has even revealed a diverse malacofauna. The diversity values per sample range from 0 to 2.2 in the section (Figure 5). Zones MZ5, MZ7, and MZ8 had the highest values, while zones MZ1–4 typically had low values (less than 1).

In the principal component analysis, the results in the correlation matrix show that the percentage variance of the first principal component is 42.63% and 16.34% of the second principal component. The two principal components cover 58.97% of the total variance, providing a good representation of the population. From the loadings of the first principal component, it is possible to estimate temperature changes in the section (Figure 5). Zones MZ2 and MZ6–9 had higher temperatures, while zones MZ2–4 had lower temperatures. Interestingly, the highest temperature was found in zone MZ6, which is considered a temperate zone. The lowest temperatures were found in zones MZ2, MZ3, and MZ4, which are classified as warm, mild, and cold, respectively. The loadings of the second principal component characterize the variation in humidity, with low values indicating a dry environment and higher values indicating a moister environment (Figure 5). In the Máza section, generally dry conditions were detected, with two more humid zones (MZ4 and MZ8) and four episodes of moist peaks (MZ1, MZ2, and MZ3) reconstructed.

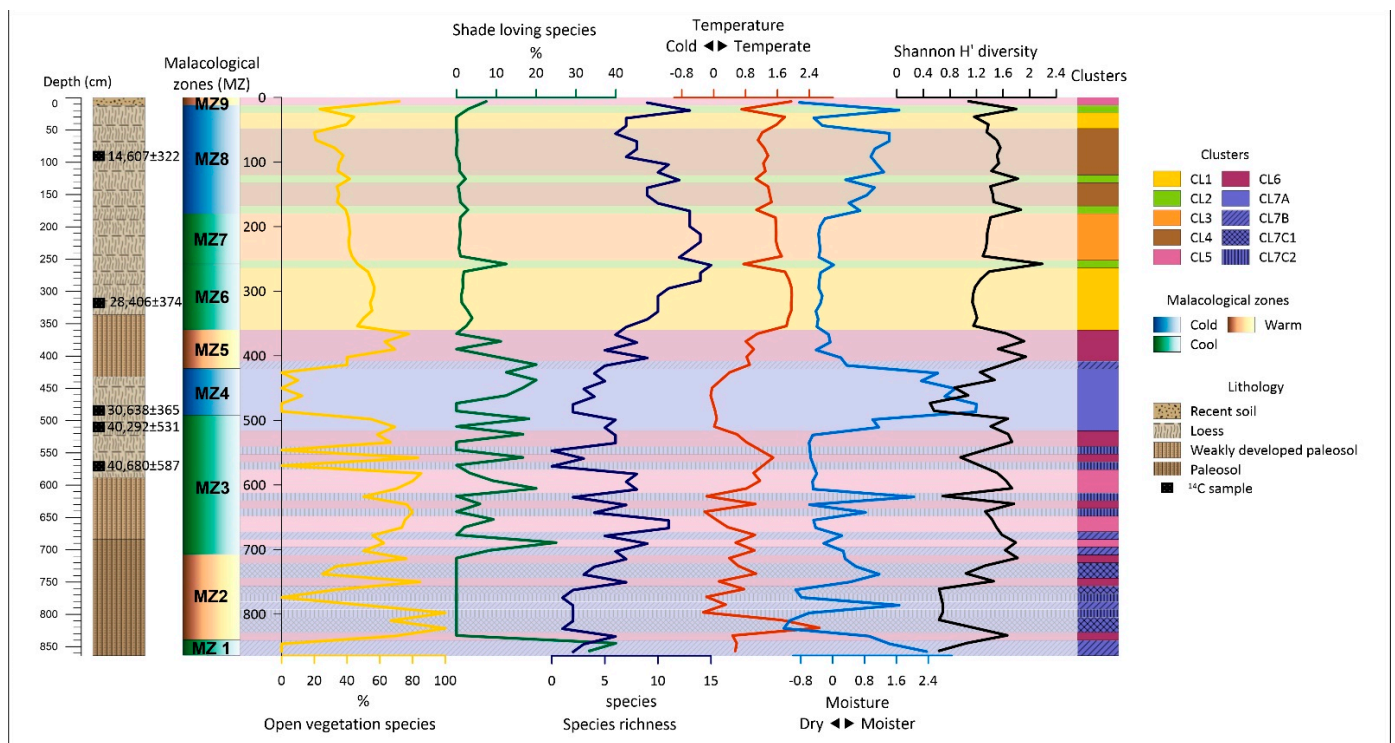


**Figure 5.** Updated results of the malacological analyses and the results of the cluster analysis.

The cluster analysis generated seven major clusters (CL1–7) that were compared with the malacological zones (MZ) defined by the previous dominance (Figure 5; Supplementary Figure S3). The cophenetic correlation value was 0.907, indicating a strong correlation. Based on the dendrogram, the samples can be divided into two large groups with a Euclidean distance of ~62. The first group includes CL1–4 and the second group CL5–7. The first group, CL1, includes 10 samples from MZ6 and MZ8, with a distance from CL2 of ~28. The second group, CL2, includes four samples scattered from MZ7 and MZ8, with a distance from CL3 of ~19. The third group, CL3, includes six samples located in MZ7, with a distance from CL4 of ~12. The fourth group, CL4, includes nine samples, all located in MZ8. The fifth group, CL5, consists of seven samples scattered in MZ3, with a distance from CL6 of ~22. The sixth group, CL6, includes 11 samples scattered in MZ2, MZ3, and MZ5, with a distance from CL7 of ~15. The seventh group, CL7, can be subdivided into sub-clusters A, B, and C, and CL7C into two parts, CL7C1 and CL7C2. The first sub-cluster, CL7A, consists of eight samples located in MZ3 and MZ4, with a distance from CL7B of ~8. The second sub-cluster, CL7B, includes six samples scattered from zones MZ1, MZ2, MZ3, and MZ5, with a distance from CL7C of ~5. The third sub-cluster, CL7C1, includes four samples exclusively from MZ2, with a distance from CL7C2 of ~4. The fourth sub-cluster, CL7C2, includes five samples originating from MZ2 and MZ3.

Based on the correspondence analysis (CA) calculation results, the first two factors account for 22.24% and 16.57%, respectively, for a total of 38.81% of the total variability (Figure 6). The theoretical threshold calculated based on the number of species is 0.0476, and species with lower values were not considered in the analysis of variability (Table 3). The distribution of CA results in the first-factor plane (X-Y axes) shows a typical “Guttman effect” in terms of species distribution, indicating that there is a specific relationship between the axes.

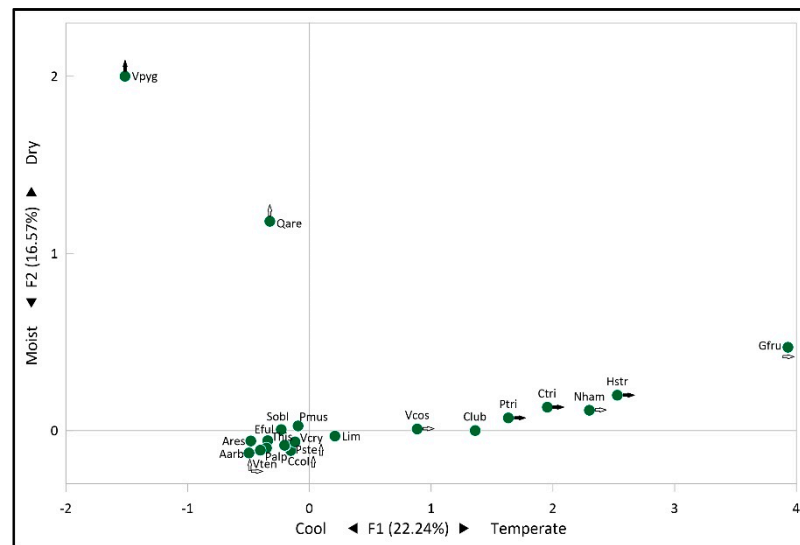


**Figure 6.** Results of the correspondence analysis based on the malacological data (black arrows: high contribution; white arrows: significant contribution; the abbreviations are discussed in Table 3).

**Table 3.** Results of the correspondence analysis of the malacological material of Máza brickyard (significant contributions—higher than the theoretical threshold (1/21) of species to the explanation of the variability of the dataset according to the first two factors).

Species	Code	Factor 1	Factor 2	Species	Code	Factor 1	Factor 2
<i>Aegopinella ressmanni</i>	Ares	-	-	<i>Pupilla muscorum</i>	Pmus	0.057	-
<i>Arianta arbustorum</i>	Aarb	-	-	<i>Pupilla sterrii</i>	Pste	0.138	0.018
<i>Chondrula tridens</i>	Ctri	2.012	-	<i>Pupilla triplicata</i>	Ptri	3.459	-
<i>Cochlicopa lubricella</i>	Club	0.177	-	<i>Quickella arenaria</i>	Qare	0.066	0.648
<i>Columella columella</i>	Ccol	0.067	0.027	<i>Succinella oblonga</i>	Sobl	-	-
<i>Euconulus fulvus</i>	Eful	0.079	-	<i>Trochulus hispidus</i>	This	0.249	0.030
<i>Granaria frumentum</i>	Gfru	1.168	-	<i>Vallonia costata</i>	Vcos	1.337	-
<i>Helicopsis striata</i>	Hstr	2.399	-	<i>Vallonia tenuilabris</i>	Vten	0.473	0.026
<i>Limacidae</i>	Llim	0.078	-	<i>Vertigo pygmaea</i>	Vpyg	0.055	6.294
<i>Nesovitrea hammonis</i>	Nham	0.524	-	<i>Vitrea crystallina</i>	Vcry	-	-
<i>Pupilla alpicola</i>	Palp	0.068	-	Theoretical threshold:		0.048	

The X-axis of the CA scatter plot (Figure 6) displays a significant contribution from *Pupilla triplicata*, *Helicopsis striata*, and *Chondrula tridens*, indicating environments that are typically dry and warm (Figure 6; Table 3). Additionally, *Granaria frumentum*, *Vallonia costata*, and *Nesovitrea hammonis* were found to have significant contributions on the positive side, while *Vallonia tenuilabris* had a significant contribution on the negative side, suggesting open and woody environments. On the positive side of the Y-axis (Figure 6; Table 3), *Vertigo pygmaea* was found to have a prominent contribution, and *Quickella arenaria* had a significant contribution, indicating cool but dry environments. On the negative side, *V. tenuilabris*, *Columella columella*, and *Pupilla sterrii* were found to have significant contributions, indicating an open, cool environment.

### 5. Discussion

The loess–paleosol profile of the Máza brickyard was examined to understand its paleoecological and sedimentological history. Five radiocarbon dates were used to calculate



age–depth models from various methods, resulting in the formation of three age–depth models and their accumulation rates (AR) (Figures 2 and 3). The OxCal’s P-sequence was chosen as the best-fitting model, and its AR graph was analyzed in detail. The model covers 60–600 cm of the 864 cm high profile, which corresponds to ~12,900–42,700 cal BP yr during the MIS3 and MIS2 periods [85,86]. The P-sequence model aided in dating sedimentological analyses and previously described malacological zones [21].

### 5.1. Accumulation Intensity and Sedimentology

The lithological description of the Mázá brickyard section has been confirmed by sedimentological investigations. The paleosol layer (864–684 cm), which is the lowest lithological unit of the section, is characterized by high magnetic susceptibility ( $\chi_{LF}$ ), organic matter, and clay content, and represents an environment of open vegetation and mild climatic conditions [87,88]. The radiocarbon dating and age–depth models suggest that this layer formed during the MIS3 (Figures 4, 5 and 7).

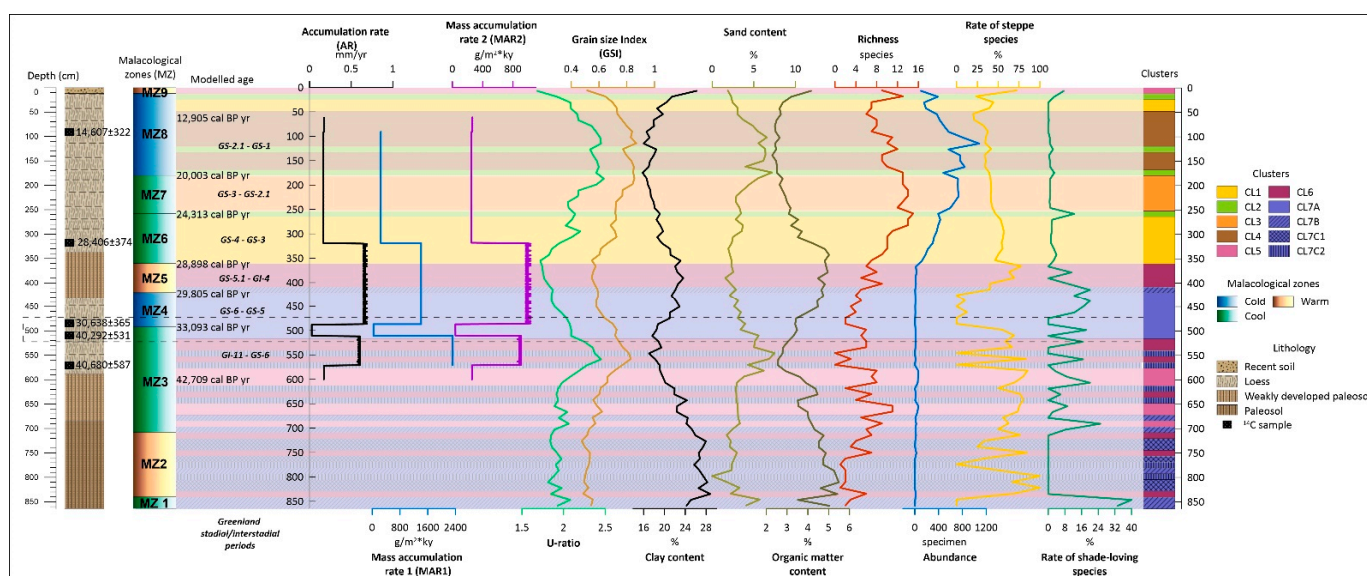


**Figure 7.** Summary figure comparing accumulation, sedimentology, and malacology results from the Mázá brickyard (dashed horizon represents the main contradiction of the section, accumulation rate was calculated from the OxCal model, MAR1 was calculated from the Table 2, MAR2 was calculated from the OxCal model).

The sedimentary record of the paleosol layer between 684 and 588 cm indicates a cooler period with decreasing magnetic susceptibility, organic matter, clay content, and low carbonate content (Figure 4). The proportion of open vegetation decreased compared to closed vegetation during this period (Figures 5 and 7). The paleosol formation period was earlier than 42,000 cal BP yr.

The loess layer (588–432 cm) overlying the paleosol layer has low magnetic susceptibility, organic matter, and clay content, but higher carbonate content (Figure 4). This layer was formed during a cool and cold period with steppe-like open vegetation in the mild period and increased humidity and closed vegetation cover in the cold period (Figure 5). The loess layer formation period spans about 12,000 years, from ~42,010 to 29,990 cal BP yr.

The calculated accumulation rate (AR) and the mass accumulation rate (MAR1 and MAR2) derived from age data and the age–depth model indicate that the loess layer was formed during two periods of extremely high accumulation (AR: 0.55 and 0.6 mm/yr; MAR1: 2400 and 1200 g/m<sup>2</sup> × ky; MAR2: 800 and 900 g/m<sup>2</sup> × ky), which were interrupted by a period of low accumulation in the section between 40,292 and 30,638 cal BP yr (AR: 0.05 mm/yr; MAR1: 36 g/m<sup>2</sup> × ky; MAR2: 40 g/m<sup>2</sup> × ky) (Figure 7). The abrupt decrease

in accumulation may suggest drier climatic conditions and increased wind erosion, but no significant erosion horizon was detected in the lithological description. Additionally, the malacological examination revealed the presence of several moisture-loving snail species (*Succinella oblonga*, *Trochulus hispidus*, Limacidae with an average 20–40% proportion) (Supplementary Figure S2) in the horizon, which decreases the probability of drier climatic conditions. Furthermore, decreased vegetation cover could result in reduced sediment accumulation. However, this could also be associated with the mobilization of particles, but the extension of open vegetation was detected at other depths in the section (e.g., Figure 5—MZ5), where the sediment accumulation did not decrease so drastically. The location of the section and its local and extra-local characteristics do not explain this phenomenon, so it is necessary to investigate the phenomenon on a larger scale, i.e., to investigate the regional scale (see Section 5.2).

The data presented in Figure 7 indicate a disparity in the composition of grains, U-ratio, and GSI between the two periods of intense accumulation. During the earlier period of reduced accumulation intensity, the grains deposited exhibited a low clay content and higher sand content, resulting in higher U-ratio and GSI values. However, this grain composition was not observed during the second period of intense accumulation. The sediment from this period had a finer grain size composition and the lowest U-ratio, which may have been due to the soil formation process that formed the poorly developed paleosol layer between 432 and 336 cm. This period is divided into three malacological zones (MZs), MZ4, MZ5, and MZ6, which cover the cold, warm, and cool zones, respectively (Figures 5 and 7; Supplementary Figure S2). MZ4 has a low proportion of typical open vegetation or shade-loving species, suggesting that a mixture of non-contiguous grassland, shrubland, and woodland may have occurred simultaneously during this period. In MZ5 and MZ6, drought-tolerant species preferring open vegetation occurred in significant proportions, indicating a dry period (Figure 5). The cold and warm but dry periods may have facilitated wind transport of finer particles in the area [42], and the significant accumulation period in this case was probably due to lower wind speeds.

The upper loess layer (336–12 cm) displays a low MS, organic matter, and clay content, with a heightened carbonate content. Additionally, the U-ratio and GSI values indicate a coarser grain size composition, which is also demonstrated by the increased sand content between ~100 and 200 cm (Figures 4 and 7). This indicates increased transport energy relations [42]. The period of sand infilling coincides with the MZ8 cold malacological zone, which lasted from ~15,000 to 21,000 cal BP yr, during the Last Glacial Maximum (LGM) [89], and more specifically, the GS-2.1 period [90] when the ice sheet boundary was closest to the study area. A potential source of sand infilling is the Inner Somogy area to the west-northwest of the site, from which wind-blown-sand movements were detected during the LGM [31].

## 5.2. Correlation with Other Loess-Paleosol Sections from the Region

To address the issue of extremely low sediment accumulation between ~40,000 and 30,000 cal BP yr, age–depth models were constructed for other loess–paleosol sections discussed previously (Figure 8). Although the reduced sediment accumulation is not unique to the Máza brickyard section, the calculated age–depth models showed a substantial decrease in accumulation for all four sections (Figure 8).

Comparing the age–depth models and reduced sediment accumulation, the closest similarity is observed between Máza, Katymár [35], and Črvenka [36] (Figures 1 and 8). In all three sections, the intensity of accumulation decreased significantly around ~40,000–38,000 cal BP yr and increased again around ~30,000 cal BP yr (Figure 8). This period of decreased dust accumulation can be placed at the end of the Marine Isotope Stage 3 (MIS3) and the transition period of the MIS3/MIS2 [85,86], including the GI-8 interstadial period [90], where warming may have been coupled with soil formation, leading to decreased accumulation.

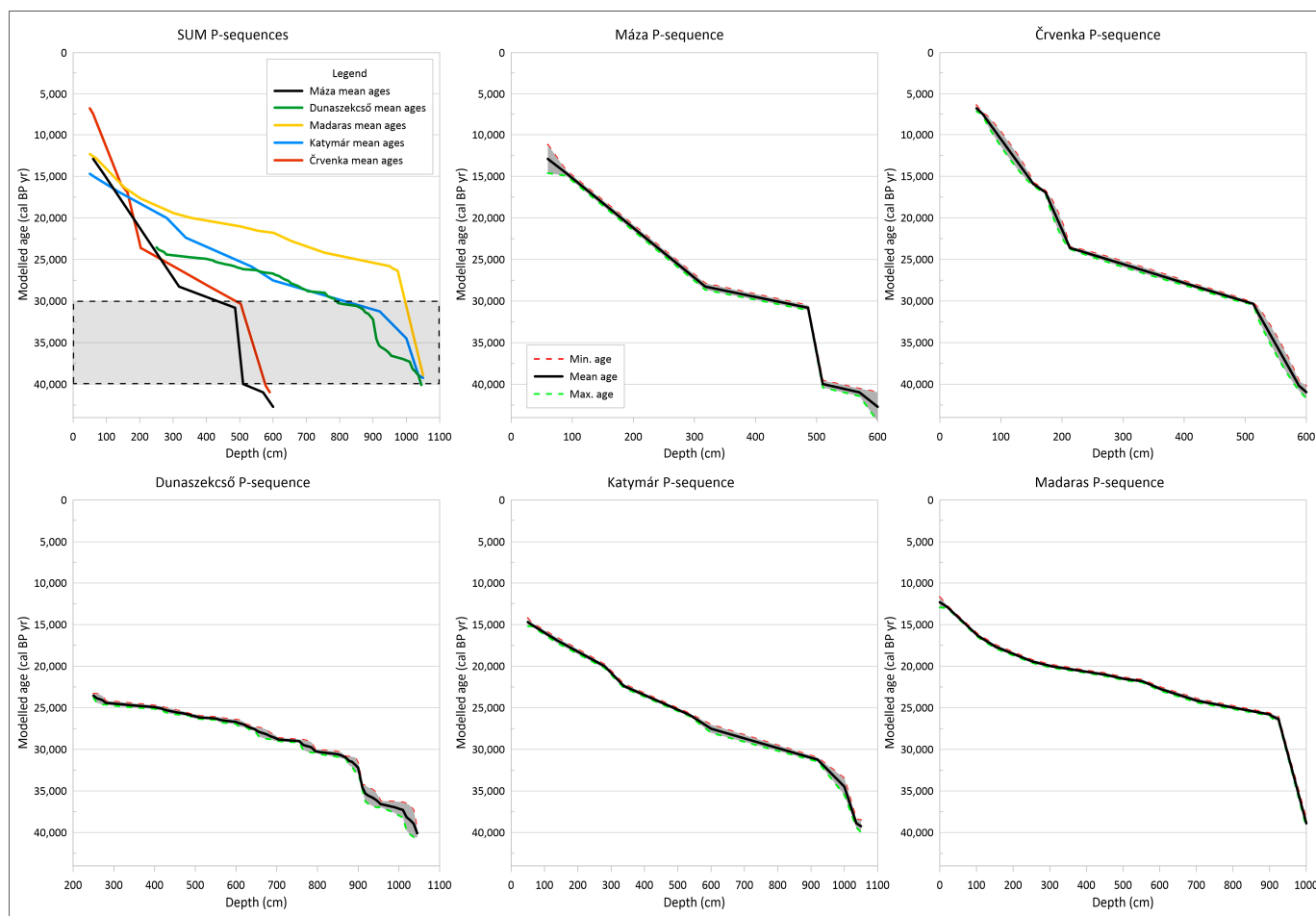


**Figure 8.** P-sequence age–depth model comparison of Máza and other nearby loess–paleosol profiles (each model was calculated in OxCal).

The Madaras and Dunaszekcső sections exhibited a similar trend. In Madaras, the low accumulation intensity persisted until approximately 26,000 cal BP yr. This may have been due to local factors or the fact that the age–depth model was constructed from 19 radiocarbon ages, which is more than the sum of the radiocarbon ages of the other three sections. Dunaszekcső had the most radiocarbon age data available, with over 100 different data points used for age–depth modeling [34]. The calculated model confirmed the low accumulation intensity between 40,000 and 30,000 cal BP yr, but there were two periods interrupted by a faster accumulation phase around 37,500–36,000 cal BP yr, during the GI-8 interstadial and GS-8 stadial [90]. The location of the section is close to the Danube River, which could provide a unique micro-environment and influence the accumulation intensity. The Máza section had the lowest sediment accumulation, which may be due to its location in a hilly area, while the other three sections are located on a more or less flat loess plateau.

### 5.3. Malacological Investigations

The interpretation of the Máza profile based on dominance has been previously published [21]. However, for the purpose of better understanding, the results must be summarized for the multi-variate analyses. From the 72 examined samples, 15,613 shells of 24 terrestrial gastropod taxa were identified. Based on their dominance ratio, 9 malacological zones (MZs) were assigned (Figure 5, Supplementary Figure S2). The age–depth model allowed for the dating of most MZs by absolute ages, making it possible to correlate them with global processes. Additionally, the PCA and cluster analyses, as well as the ratio

of open vegetation-preferring and shade-loving species, and the species richness, were calculated to supplement the previous results.

The dominance ratios of the lowermost and oldest MZ1 (864–840 cm) indicated a cool climate with a relatively low abundance. This zone was considered a transition zone between the lower paleosol and the unrevealed loess layers. The ratio of shade-loving species was the highest here, with 0% of open vegetation preferring (steppe) species. This suggests a relatively high rate of closed vegetation, such as an open parkland-type paleovegetation.

The second zone (MZ2 between 840 and 708 cm) overlaid in the paleosol layer and could be described as a “warm” period with a significant ratio of steppe species and the disappearance of shade-loving species. This warmer period could be correlated with the 12th Greenland Interstadial (GI-12), which occurred between 48,340 and 44,560 cal BP yr [90] during the MIS 3 [85,86].

The cool zone of MZ3 extends between 708 and 492 cm and is characterized by species that thrive in warmth and moderate temperatures, with a minor presence of cold-resistant and cold-loving species. The proportion of steppe species was higher, while the ratio of shade-loving species varied, but with a predominance of steppe species. It is possible that MZ3 is another transitional zone, supported by its higher species richness. The age of this zone can be estimated using the calculated age–depth model, and the 600–492 cm stage of the zone falls within the model’s range. This stage’s age is estimated to be between 42,709 and 33,093 cal BP yr.

The MZ4 zone (492–420 cm) represents the first stage of cold climate, which can be dated back to 33,093–29,805 cal BP yr, overlapping with the GS-5 stadial [90]. The ratio of cold-resistant and cold-loving species was around 80–90% (50–60% cold-loving), indicating a severe cold period in MZ4 (Figure 5; Supplementary Figure S2). The proportion of steppe species was minimal, while the ratio of shade-loving species was 0–10%. Based on the species composition [21], the paleoenvironment could have resembled today’s alpine meadows with scattered tree groups. The malacological zone of MZ4 evolved during the 3rd Heinrich event (H3) [91], as per the paleoecological and age data.

MZ5 (420–360 cm) was a warmer period overlapping the GI-4 interstadial [90], between 29,805 and 28,898 cal BP yr. The climate transitioned from a colder to a warmer period, as evidenced by the upper weakly developed paleosol layer. The ratio of steppe species increased rapidly, fluctuating between 40 and 80%, while the shade-loving species ratio fell below 20%. This indicates that the steppe environment with tree groups returned during this period.

The next two zones, MZ6 (360–252 cm) and MZ7 (252–180 cm), covered approximately 9,000 years (from 28,898 to 24,313 cal BP yr for MZ6 and from 24,313 to 20,003 cal BP yr for MZ7) and can be discussed together. During this time, the climate varied in its dominance of the mesophilous *Pupilla muscorum* and the cold-resistant *Succinella oblonga* and *Trochulus hispidus*. The steppe/shade-loving species ratio was 40–60%/0–10%, indicating the main steppe environment with some scattered tree spots in the area. MZ6 and MZ7 were formed during the GS-3 and GS-2 stadials [90] in the MIS2 [85,86], and the varying dominance of species indicated the highest richness in these zones, fluctuating between 8 and 15.

After the cool periods, a cold period occurred (MZ8: 180–12 cm; 20,003–12,905 cal BP yr), although temperatures were not as low as during MZ4. The dominance ratio of cold-loving and cold-resistant species was around 80%, with most of these values being added by cold-resistant species [21]. The steppe/shade-loving species ratio remained relatively stable at 30–50%/0–5%, indicating a lack of woods, with perhaps a few tree groups present during this period (Figure 5). Given the age of this zone, it is possible that this cold period corresponds to the H1 Heinrich event [91].

The uppermost zone, situated just below the modern soil horizon, serves as the most recent portion of the sequence (MZ9: 12–0 cm). This zone exhibits substantial variations in the dominance ratio, suggesting a warming phase, possibly marking the onset of the Holocene epoch. Concurrently, both the steppe and shade-loving ratios experienced growth,



indicating an expanding woodland region and a steppe ecosystem characterized by the presence of trees.

### Cluster Analysis

After conducting an in-depth analysis of the cluster results (Figure 5; Supplementary Table S2; Supplementary Figure S3), it is evident that the seven identified clusters display unique malacological compositions.

The ten samples of cluster CL1 comprise 14 species, with an average of 267 individuals and an average species richness of 9.9. The most prevalent species in the cluster are *Pupilla muscorum*, which prefers open vegetation and constitutes 49.11% of the population, *Trochulus hispidus*, which prefers closed vegetation and represents 33.6% of the population, and *Succinella oblonga*, which is cold-resistant and prefers a wet environment, comprising 10.11% of the population. These three species were present in all samples of the cluster. Additionally, *Vallonia tenuilabris*, *Pupilla sterrii*, and *Vallonia costata*, which are cold resistant, were present in significant numbers but in low proportions. It should be noted that the cluster also included *Columella columella* and several species with a preference for closed vegetation, such as *Euconulus fulvus* and *Vitrea crystallina*. These results suggest that cluster CL1, due to the high proportion of *P. muscorum*, is essentially open vegetation, interspersed with areas of forest patches of smaller to larger size, typically characterized by a more humid microclimate. The average temperature in this cluster may have been lower and rather cool, due to the presence of cold-loving and cold-resistant species, particularly *V. tenuilabris*. The CL1 cluster covers the MZ6 malacozone (360–264 cm; between 28,898 and 24,313 cal BP yr) and also appears in MZ8 (48–24 cm; younger than 14,000 cal BP yr).

The CL2 cluster comprises a total of four samples, each positioned between the other clusters. The samples are arranged from 264 to 252 cm at the MZ6–MZ7 boundary, 180 to 168 cm at the MZ7–MZ8 boundary, 132 to 120 cm in MZ8, and 24 to 12 cm at the MZ8–MZ9 boundary. The cluster contains 16 species, with an average of 473 individuals and an average species richness of 13.25. The most prevalent species in the cluster are *S. oblonga* (4 samples; 25.66%), *P. muscorum* (4 samples; 18.92%), *T. hispidus* (4 samples; 15.9%), and *P. sterrii* (4 samples; 9.27%). The mesophilous *Vallonia pulchella* is present in all samples, indicating a higher humidity environment, along with *S. oblonga* and *T. hispidus*. Moreover, the cluster has a larger colony of cold-loving species, including *V. tenuilabris* (4 samples, 6.23%; *C. columella*: 3 samples, 5.17%; *Pupilla alpicola*: 3 samples, 2.13%). The cluster also contains a colony preferring closed vegetation (*V. crystallina*: 4 samples, 3.18%, Limacidae: 4 samples, 1.73%; *E. fulvus*: 3 samples, 0.21%) and a warmth-loving colony (*Pupilla triplicata*: 2 samples, 3.59%; *Cochlicopa lubricella*: 2 samples, 0.16%; *Chondrula tridens*: 2 samples, 0.12%). The high species richness and the co-occurrence of species with diverse environmental and climatic requirements suggest that the CL2 cluster may represent a transitional horizon between other clusters and malacozones. This cluster is characterized by higher humidity, open vegetation interspersed with more extensive patches of forest, and higher humidity.

The six samples of the CL3 cluster adequately represent the MZ7 malacozone, encompassing a range of 252–180 cm and 24,313–20,003 cal BP yr. The cluster boasts an average of 700 individuals and 13.1 species per sample. Of the 14 species present, 10 are found in all cluster samples, with the remaining 4 being more prominent: *T. hispidus* at 44.5%, *P. muscorum* at 34.16%, *S. oblonga* at 8.03%, and *P. sterrii* at 6.96%. *V. tenuilabris* accounts for 3.19% of the cluster species, while the remaining species make up less than 1%. It is noteworthy that *C. columella* and *P. alpicola*, which prefer low temperatures, as well as *E. fulvus*, Limacidae, and *V. crystallina*, which thrive in shaded areas, are included in this group. The prevalence of cold-tolerant and cold-loving species suggests a period of lower average temperatures, but not unusually cold ones. The increased humidity during this time was accompanied by extensive forested areas, but they were not entirely closed off.

Cluster CL4 comprises nine samples located solely in the MZ8 zone, encompassing an age range from 19,285 to 17,130 cal BP yr and 120 to 48 cm, and 16,411 to ~12,000 cal BP yr, respectively. The species richness and average abundance in CL4 are comparable to

those in CL3, with 15 species and 679 individuals, respectively. The species distribution in CL4 is more balanced than in CL3, with *S. oblonga* accounting for 39.44% of the total, followed by *P. muscorum* at 26.9%, and *T. hispidus* at 18.69%. *V. tenuilabris*, *C. columella*, and *P. sterrii* are other notable species found in all samples of the cluster, with percentages of 5.15%, 4.69%, and 4.43%, respectively. The remaining species were found in fewer than 1% of the samples. A striking correlation was discovered between CL3 and CL4, despite their differences in species composition. The top six species in both clusters are identical, albeit in a different order. In CL4, the proportion of cold-preferring *V. tenuilabris* and *C. columella* is higher, while the proportion of cold-tolerant *S. oblonga* is also significantly greater than in CL3. This suggests that CL4 represents an environment with lower mean temperature and higher humidity, as indicated by the temperature and humidity curves depicted in Figure 5.

The low-abundance samples in CL5 and the additional clusters are limited. For CL5, the average abundance per sample is 58 individuals, and the species richness is 16 species, which is the highest among all clusters, with an average of 9 species per sample. The 7 samples in the cluster are primarily from the lower section of the MZ3 zone (696–684 cm, 672–648 cm, 612–576 cm), and include the uppermost 12–0 cm of the section. The most abundant gastropod species in the cluster are *P. muscorum* (7 samples, 30.38%), *V. costata* (7 samples, 23.44%), *P. triplicata* (6 samples, 10.09%), and Limacidae (7 samples, 9.68%). Additionally, *T. hispidus* (6 samples, 8.45%), *P. sterrii* (5 samples, 6.19%), *V. pulchella* (6 samples, 4.34%), and *Chondrula tridens*, which is present in all samples but with an average abundance of only 2.31%, are also more abundant. The cluster is characterized by the dominance of cold-resistant and cryophilous species, with a higher proportion of species preferring open vegetation than in CL4. This is supported by the presence of the thermophilous, distinctly steppe species *C. tridens* in all samples. In contrast to CL2, the high species richness in this cluster does not indicate a transitional cluster, but rather an environmental situation with lower humidity and higher average temperatures, with a predominance of species preferring open vegetation (about 70%).

The samples within CL6 are distributed in the lower-central part of the section, spanning from 840 to 828 cm, 756 to 744 cm, 720 to 708 cm, 636 to 624 cm, and 564 to 552 cm, with an age range of ~40,546 cal BP yr. Additionally, there are two samples with an age range of 540–504 cm and 408–360 cm, corresponding to 39,827–36,701 cal BP yr and 29,601–28,635 cal BP yr, respectively. The cluster contains a total of 12 samples, with an average of 6.25 species per sample and 17 individuals per sample. The most abundant species in the cluster are *P. muscorum* (21.23%) and *P. triplicata* (21.61%), both of which prefer open vegetation and mesophilous conditions. Other species present in higher proportions include *T. hispidus* (9 samples, 12.98%), *V. costata* (7 samples, 5.88%), *S. oblonga* (6 samples, 7.55%), and *C. tridens* (7 samples, 5.88%). The cluster is found in malacological zones MZ2, MZ3, and MZ5, two of which (MZ3 and MZ5) are considered “warm” based on dominance ratios (Figure 5) [21]. Therefore, the species composition of this cluster suggests that it represents climatic zones with open vegetation and higher average temperatures in the development history of the section.

The CL7 cluster generally encompasses samples from the lower portion of the section. It can be further divided into four subclusters, each characterized by a low number of species (4–9) and low abundance (2–7 individuals/sample). The seven contiguous samples of cluster 7A (504–420 cm—36,701–29,841 cal BP yr) span approximately 6,860 years of the developmental history of the section. This cluster covers the top of the MZ3 zone and the entire MZ4 zone. The highest proportion (also for the entire section) of cold- and moisture-loving *Columella columella* (7 samples, 55.56%) characterizes this cluster. Additionally, the cold-tolerant hygrophilous *S. oblonga* (6 samples, 18.81%), the moisture-tolerant Limacidae species (5 samples, 11.41%), the shade-loving, cold-tolerant *T. hispidus* (2 samples, 3.11%), and, as a counterbalance, the thermophilous *P. triplicata* (3 samples, 7.11%) also characterize the cluster in a more significant proportion. The high proportion of cold-loving and cold-tolerant species, the high proportion of moisture-loving species, and the greater prevalence

of closed vegetation indicate that the cluster represents the coldest and most humid period of the section (Figure 5), where the prevalence of closed vegetation surpassed that of open vegetation.

Cluster 7B encompasses the entire MZ1 zone and also comprises samples from MZ2, MZ3, and MZ5. *S. oblonga* (6 samples, 37.31%) was the most prevalent species in the cluster, followed by comparable proportions of Limacidae (3 samples, 13.61%), *P. muscorum* (3 samples, 12.59%), *C. tridens* (3 samples, 11.57%), and *T. hispidus* (3 samples, 10.37%), which are primarily indicative of a humid environment. The species composition and their proportions show similarities with cluster CL2, which was characterized as a fauna-transition cluster. This may also be the case here and is most pronounced at the transition between CL7A and CL5 (MZ4 and MZ5), where zones of low to high mean temperature are in contact.

Cluster 7C can be further subdivided into two subclusters, which have the general characteristic of containing samples with very low abundance. Cluster 7C1 is restricted to the MZ2 zone. The overwhelmingly dominant species is *P. muscorum* (5/5 samples, 48.33%), which is typical of open vegetation environments. The presence of *Quickella arenaria* (5/4 samples, 31.67%) and *S. oblonga* (5/2 samples, 16.67%) indicates moister conditions. The environment was characterized by open vegetation and alternating dry and damp areas. Cluster 7C2 contains a similar proportion of species with different environmental requirements, so no meaningful information is available for this cluster.

Taking into account the results of the cluster analysis, a much more detailed picture of the changes in the malacofauna can be obtained, including the changes in the environmental factors influencing its evolution. The cluster analysis conducted in the Máza brickyard area reveals that it differs from the nearby extralocal (Villánykövesd: [21]) and regional-scale (Katymár: [35]; Madaras: [19]; Črvenka: [25]; Szeged-Öthalom: [24]) loess–paleosol sections in terms of lower average temperatures and higher humidity. This is evidenced by the high proportion of moisture-loving species such as *Succinella oblonga*, *Trochulus hispidus*, *Vallonia pulchella*, as well as shade-loving species, and the lower mean temperature by the presence of cold-tolerant (*S. oblonga*, *T. hispidus*, *Pupilla sterrii*) and cold-loving (*Vallonia tenuilabris*, *Columella columella*, *Pupilla alpicola*) species. The presence of thermophilous species with a high contribution to the correspondence analysis is significant (Figure 6; Table 3). Although *Granaria frumentum*, *Helicopsis striata*, *Chondrula tridens*, and *Pupilla triplicata* are not significant species in the Máza malacofauna as a whole, their presence is associated with warming periods and the emergence of open vegetation.

Three of the clusters stand out from the rest. These include the CL2 cluster that shows a four-level transition horizon between CL1/CL3 (264–252 cm, 24,649–23,956 cal BP yr), CL3/CL4 (180–168 cm, 19,797–19,105 cal BP yr), and the CL4 cluster (132–120 cm, 17,029–16,331 cal BP yr) and CL1/CL6 (24–12 cm, around the Pleistocene-Holocene boundary). Notably, all the CL2 cluster elements were formed during stadial periods, such as the CL1/CL3 transition during GS-3, the CL3/CL4 transition during GS-2.1b, the CL4 transition during GS-2.1a, and the CL1/CL6 transition during GS-1 stadials [90]. Cluster CL6 represents the warmest periods of the section, where species that typically prefer open vegetation (thermophilous and mesophilous) were typically most abundant. It also indicates the expansion of the steppe. On the other hand, Cluster CL7A contains the highest proportion of cold-loving and cold-tolerant species, together with several closed vegetation species, representing the coolest and highest humidity period of the section between 36,701 and 29,841 cal BP yr, between GS-8 and GS-5 stadials [90]. The NGRIP data show that the interstadials GI-7, 6, 5.2, and 5.1 also belong to this time frame, but there is no trace of these in the Máza section, and the local conditions in the study area are unlikely to reveal any trace of warming.

## 6. Conclusions

The chronological, paleoecological, and sedimentological analyses allowed for the unraveling of the sediment development and the malacofauna evolution in the vicinity

of Máza brickyard in the past ~45,000–50,000 years. The results of these analyses provide several conclusions regarding the evolution and characteristics of the region during this time period.

It is crucial to possess a reliable age–depth model that is well suited for the available radiocarbon ages. In the instance of Máza brickyard, OxCal’s P-sequence was chosen. However, only a portion of the 864 cm high profile (60–600 cm) could be modeled due to the scarcity of additional radiocarbon ages. Therefore, to determine the best-fitting model, radiocarbon sampling should be conducted as close to the top and bottom of the investigated profile as possible. When examining the P-sequence models of different profiles (Figure 8), only the P-sequence of the Madaras profile diverged from the others. At Madaras, 19 radiocarbon samples were used for calculations, in contrast, fewer samples—only 5 samples at Máza, 6 samples at Črvenka, and 9 samples at Katymár—were available for modeling from the other profiles. The reason for the difference was that the P-sequence of Madaras was more precise than the others. In summary, 5–10 or more radiocarbon samples are necessary for more precise models.

The period between approximately 40,000 and 30,000 cal BP years could be characterized as the lowest accumulation period (AR: ~0.05 mm/yr; MAR1: 36 g/m<sup>2</sup> × ky; MAR2: 40 g/m<sup>2</sup> × ky) (Figures 3 and 7). The low values might indicate eroded or reworked sediment, but the similarity to the other P-sequences contradicts this hypothesis or suggests a common erosion event in the broader region of the South Carpathian Basin at the end of MIS3 [85,86], although the probability is low. It is more likely that the decreasing accumulation intensity resulted in common low sedimentation rates.

Multivariate statistical analyses contribute significantly to the interpretations and conclusions derived from malacological studies. The cluster analysis, in particular, enables a more refined paleoecological reconstruction, presenting a clearer picture of the evolutionary history of the studied section. In the instance of Máza brickyard, this approach has delineated transition horizons between cooler and warmer, as well as drier and moister episodes, and has also revealed that during the last glacial period, the area of the brickyard experienced high humidity and relatively cool average temperatures.

**Supplementary Materials:** The following supporting information can be downloaded at <https://www.mdpi.com/article/10.3390/quat7030035/s1>, Figure S1: The iteration data of the Bacon age–depth model calculated in Máza brickyard profile; Figure S2: The dominance-based malacological results and malacological zones (MZ) of Máza brickyard based on Molnár et al., 2019; Figure S3: Dendrogram of the cluster analysis employed on malacological results of Máza loess–paleosol section (numbers on the right side of the dendrogram represents the sample numbers); Table S1: Logarithmic transformation (“Rousseau code”) of the snail abundance results of Máza brickyard; Table S2: Detailed description of the cluster analysis focusing on the percentage of snail species (for abbreviations, see Table 3).

**Author Contributions:** Conceptualization, D.M. and P.S.; methodology, D.M.; software, D.M.; validation, M.M., P.S. and D.M.; formal analysis, L.M.; investigation, L.M. and D.M.; resources, P.S. and M.M.; data curation, D.M.; writing—original draft preparation, D.M.; writing—review and editing, D.M. and L.M.; visualization, D.M.; supervision, P.S.; project administration, D.M. and L.M.; funding acquisition, P.S. and M.M. All authors have read and agreed to the published version of the manuscript.

**Funding:** This research was funded by the Hungarian Government, the Ministry of Human Capacities (20391-3/2018/FEKUSTRAT), and the European Regional Development Fund (GINOP-2.3.2-15-2016-00009 ‘ICER’). D. Molnár would like to thank the support of the Hungarian National Excellence Programme grant NTP-NFTÖ-19-B-0158.

**Data Availability Statement:** The raw data supporting the conclusions of this article will be made available by the authors upon request.

**Conflicts of Interest:** The authors declare no conflicts of interest.



## References

- Kukla, G.J. Pleistocene Land—Sea Correlations I. Europe. *Earth-Sci. Rev.* **1977**, *13*, 307–374. [[CrossRef](#)]
- Chen, F.H.; Bloemendal, J.; Wang, J.M.; Li, J.J.; Oldfield, F. High-Resolution Multi-Proxy Climate Records from Chinese Loess: Evidence for Rapid Climatic Changes over the Last 75 Kyr. *Palaeogeogr. Palaeoclim. Palaeoecol.* **1997**, *130*, 323–335. [[CrossRef](#)]
- Carter-Stiglitz, B.; Banerjee, S.K.; Gourelan, A.; Oches, E. A Multi-Proxy Study of Argentina Loess: Marine Oxygen Isotope Stage 4 and 5 Environmental Record from Pedogenic Hematite. *Palaeogeogr. Palaeoclim. Palaeoecol.* **2006**, *239*, 45–62. [[CrossRef](#)]
- Torrent, J.; Liu, Q.; Bloemendal, J.; Barrón, V. Magnetic Enhancement and Iron Oxides in the Upper Luochuan Loess–Paleosol Sequence, Chinese Loess Plateau. *Soil Sci. Soc. Am. J.* **2007**, *71*, 1570–1578. [[CrossRef](#)]
- Haberlah, D.; Williams, M.A.J.; Halverson, G.; McTainsh, G.H.; Hill, S.M.; Hrstka, T.; Jaime, P.; Butcher, A.R.; Glasby, P. Loess and Floods: High-Resolution Multi-Proxy Data of Last Glacial Maximum (LGM) Slackwater Deposition in the Flinders Ranges, Semi-Arid South Australia. *Quat. Sci. Rev.* **2010**, *29*, 2673–2693. [[CrossRef](#)]
- Sun, Y.; He, L.; Liang, L.; An, Z. Changing Color of Chinese Loess: Geochemical Constraint and Paleoclimatic Significance. *J. Asian Earth Sci.* **2011**, *40*, 1131–1138. [[CrossRef](#)]
- Bird, A.; Stevens, T.; Rittner, M.; Vermeesch, P.; Carter, A.; Andò, S.; Garzanti, E.; Lu, H.; Nie, J.; Zeng, L.; et al. Quaternary Dust Source Variation across the Chinese Loess Plateau. *Palaeogeogr. Palaeoclim. Palaeoecol.* **2015**, *435*, 254–264. [[CrossRef](#)]
- Tecsa, V.; Mason, J.A.; Johnson, W.C.; Miao, X.; Constantin, D.; Radu, S.; Magdas, D.A.; Veres, D.; Marković, S.B.; Timar-Gabor, A. Latest Pleistocene to Holocene Loess in the Central Great Plains: Optically Stimulated Luminescence Dating and Multi-Proxy Analysis of the Enders Loess Section (Nebraska, USA). *Quat. Sci. Rev.* **2020**, *229*, 106130. [[CrossRef](#)]
- Rousseau, D.-D.; Puisségur, J.-J. Climatic Interpretation of Terrestrial Malacofaunas of the Last Interglacial in Southeastern France. *Palaeogeogr. Palaeoclim. Palaeoecol.* **1999**, *151*, 321–336. [[CrossRef](#)]
- Antoine, P.; Rousseau, D.-D.; Zöller, L.; Lang, A.; Munaut, A.-V.; Hatté, C.; Fontugne, M. High-Resolution Record of the Last Interglacial–Glacial Cycle in the Nussloch Loess–Palaeosol Sequences, Upper Rhine Area, Germany. *Quat. Int.* **2001**, *76–77*, 211–229. [[CrossRef](#)]
- Moine, O.; Rousseau, D.-D.; Antoine, P. The Impact of Dansgaard–Oeschger Cycles on the Loessic Environment and Malacofauna of Nussloch (Germany) during the Upper Weichselian. *Quat. Res.* **2008**, *70*, 91–104. [[CrossRef](#)]
- Alexandrowicz, W.P.; Dmytruk, R. Molluscs in Eemian–Vistulian Deposits of the Kolodiv Section, Ukraine (East Carpathian Foreland) and Their Palaeoecological Interpretation. *Geol. Q.* **2007**, *51*, 173–178.
- Újvári, G.; Kovács, J.; Varga, G.; Raucsik, B.; Marković, S.B. Dust Flux Estimates for the Last Glacial Period in East Central Europe Based on Terrestrial Records of Loess Deposits: A Review. *Quat. Sci. Rev.* **2010**, *29*, 3157–3166. [[CrossRef](#)]
- Zeeden, C.; Kels, H.; Hambach, U.; Schulte, P.; Protze, J.; Eckmeier, E.; Marković, S.B.; Klasen, N.; Lehmkuhl, F. Three Climatic Cycles Recorded in a Loess–Palaeosol Sequence at Semlac (Romania)—Implications for Dust Accumulation in South-Eastern Europe. *Quat. Sci. Rev.* **2016**, *154*, 130–142. [[CrossRef](#)]
- Song, Y.; Guo, Z.; Marković, S.; Hambach, U.; Deng, C.; Chang, L.; Wu, J.; Hao, Q. Magnetic Stratigraphy of the Danube Loess: A Composite Titel–Stari Slankamen Loess Section over the Last One Million Years in Vojvodina, Serbia. *J. Asian Earth Sci.* **2018**, *155*, 68–80. [[CrossRef](#)]
- Sümegei, P.; Gulyás, S.; Molnár, D.; Sümegei, B.P.; Almond, P.C.; Vandenberghe, J.; Zhou, L.; Pál-Molnár, E.; Töröcsik, T.; Hao, Q.; et al. New Chronology of the Best Developed Loess/Paleosol Sequence of Hungary Capturing the Past 1.1 Ma: Implications for Correlation and Proposed Pan-Eurasian Stratigraphic Schemes. *Quat. Sci. Rev.* **2018**, *191*, 144–166. [[CrossRef](#)]
- Csonka, D.; Bradák, B.; Barta, G.; Szeberényi, J.; Novothny, Á.; Végh, T.; Süle, G.T.; Horváth, E. A Multi-Proxy Study on Polygenetic Middle-to Late Pleistocene Paleosols in the Hévízgyörk Loess–Paleosol Sequence (Hungary). *Quat. Int.* **2020**, *552*, 25–35. [[CrossRef](#)]
- Hupuczi, J.; Molnár, D.; Galović, L.; Sümegei, P. Preliminary Malacological Investigation of the Loess Profile at Šarengrad, Croatia. *Open Geosci.* **2010**, *2*, 57–63. [[CrossRef](#)]
- Hupuczi, J.; Sümegei, P. The Late Pleistocene Paleoenvironment and Paleoclimate of the Madaras Section (South Hungary), Based on Preliminary Records from Mollusks. *Open Geosci.* **2010**, *2*, 64–70. [[CrossRef](#)]
- Molnár, D.; Hupuczi, J.; Galović, L.; Sümegei, P. Preliminary Malacological Investigation on the Loess Profile at Zmajevac, Croatia. *Open Geosci.* **2010**, *2*, 52–56. [[CrossRef](#)]
- Molnár, D.; Sümegei, P.; Fekete, I.; Makó, L.; Sümegei, B.P. Radiocarbon Dated Malacological Records of Two Late Pleistocene Loess–Paleosol Sequences from SW-Hungary: Paleoecological Inferences. *Quat. Int.* **2019**, *504*, 108–117. [[CrossRef](#)]
- Sümegei, P. *Loess and Upper Paleolithic Environment in Hungary: An Introduction to the Environmental History of Hungary*; Aurea: Nagykovacs, Hungary, 2005; ISBN 978-963-218-212-4.
- Sümegei, P.; Gulyás, S.; Csökmei, B.; Molnár, D.; Hambach, U.; Stevens, T.; Markovic, S.B.; Almond, P.C. Climatic Fluctuations Inferred for the Middle and Late Pleniglacial (MIS 2) Based on High-Resolution (~ca. 20 y) Preliminary Environmental Magnetic Investigation of the Loess Section of the Madaras Brickyard (Hungary). *Cent. Eur. Geol.* **2012**, *55*, 329–345. [[CrossRef](#)]
- Sümegei, P.; Náfrádi, K.; Molnár, D.; Sávai, S. Results of Paleoecological Studies in the Loess Region of Szeged–Óthalom (SE Hungary). *Quat. Int.* **2015**, *372*, 66–78. [[CrossRef](#)]
- Sümegei, P.; Marković, S.B.; Molnár, D.; Sávai, S.; Náfrádi, K.; Szelepcsényi, Z.; Novák, Z. Črvenka Loess–Paleosol Sequence Revisited: Local and Regional Quaternary Biogeographical Inferences of the Southern Carpathian Basin. *Open Geosci.* **2016**, *8*, 390–404. [[CrossRef](#)]

26. Sümegi, P.; Gulyás, S.; Molnár, D.; Szilágyi, G.; Sümegi, B.P.; Törőcsik, T.; Molnár, M. <sup>14</sup>C Dated Chronology of the Thickest and Best Resolved Loess/Paleosol Record of the LGM from SE Hungary Based on Comparing Precision and Accuracy of Age-Depth Models. *Radiocarbon* **2020**, *62*, 403–417. [[CrossRef](#)]
27. Bösken, J.; Sümegi, P.; Zeeden, C.; Klasen, N.; Gulyás, S.; Lehmkuhl, F. Investigating the Last Glacial Gravettian Site ‘Ságvár Lyukas Hill’ (Hungary) and Its Paleoenvironmental and Geochronological Context Using a Multi-Proxy Approach. *Palaeogeogr. Palaeoclim. Palaeoecol.* **2018**, *509*, 77–90. [[CrossRef](#)]
28. Molnár, D.; Sümegi, P.; Makó, L.; Cseh, P.; Zeeden, C.; Nett, J.; Lehmkuhl, F.; Törőcsik, T.; Sümegi, B.P. Palaeoecological Background of the Upper Palaeolithic Site of Ságvár, Hungary: Radiocarbon-dated Malacological and Sedimentological Studies on the Late Pleistocene Environment. *J. Quat. Sci.* **2021**, *36*, 1353–1363. [[CrossRef](#)]
29. Molnár, D.; Makó, L.; Cseh, P.; Sümegi, P.; Fekete, I.; Galović, L. Middle and Late Pleistocene Loess-Paleosol Archives in East Croatia: Multi-Proxy Paleoecological Studies on Zmajevac and Šarengrad II Sequences. *Stud. Quat.* **2021**, *38*, 3–17. [[CrossRef](#)]
30. Lehmkuhl, F.; Nett, J.J.; Pötter, S.; Schulte, P.; Sprafke, T.; Jary, Z.; Antoine, P.; Wacha, L.; Wolf, D.; Zerboni, A.; et al. Loess Landscapes of Europe—Mapping, Geomorphology, and Zonal Differentiation. *Earth-Sci. Rev.* **2021**, *215*, 103496. [[CrossRef](#)]
31. Dövényi, Z. *Magyarország Kistájainak Katasztere (Inventory of Microregions in Hungary)*; Hungarian Academy of Sciences: Budapest, Hungary, 2010; ISBN 978-963-9545-29-8.
32. Újvári, G.; Molnár, M.; Novothny, Á.; Páll-Gergely, B.; Kovács, J.; Várhegyi, A. AMS <sup>14</sup>C and OSL/IRSL Dating of the Dunaszekcső Loess Sequence (Hungary): Chronology for 20 to 150 Ka and Implications for Establishing Reliable Age–Depth Models for the Last 40 Ka. *Quat. Sci. Rev.* **2014**, *106*, 140–154. [[CrossRef](#)]
33. Újvári, G.; Molnár, M.; Páll-Gergely, B. Charcoal and Mollusc Shell <sup>14</sup>C-Dating of the Dunaszekcső Loess Record, Hungary. *Quat. Geochronol.* **2016**, *35*, 43–53. [[CrossRef](#)]
34. Újvári, G.; Stevens, T.; Molnár, M.; Demény, A.; Lambert, F.; Varga, G.; Jull, A.J.T.; Páll-Gergely, B.; Buylaert, J.-P.; Kovács, J. Coupled European and Greenland Last Glacial Dust Activity Driven by North Atlantic Climate. *Proc. Natl. Acad. Sci. USA* **2017**, *114*, E10632–E10638. [[CrossRef](#)] [[PubMed](#)]
35. Sümegi, P.; Molnár, D.; Gulyás, S.; Náfrádi, K.; Sümegi, B.P.; Törőcsik, T.; Persaits, G.; Molnár, M.; Vandenberghe, J.; Zhou, L. High-Resolution Proxy Record of the Environmental Response to Climatic Variations during Transition MIS3/MIS2 and MIS2 in Central Europe: The Loess-Paleosol Sequence of Katymár Brickyard (Hungary). *Quat. Int.* **2019**, *504*, 40–55. [[CrossRef](#)]
36. Sümegi, P.; Gulyás, S. Some Notes on the Interpretation and Reliability of Malacological Proxies in Paleotemperature Reconstructions from Loess—Comments to Obreht et al. ‘s “A Critical Reevaluation of Paleoclimate Proxy Records from Loess in the Carpathian Basin.”’ *Earth-Sci. Rev.* **2021**, *221*, 103675. [[CrossRef](#)]
37. Molnár, M.; Janovics, R.; Major, I.; Orsovski, J.; Gönczi, R.; Veres, M.; Leonard, A.G.; Castle, S.M.; Lange, T.E.; Wacker, L.; et al. Status Report of the New AMS <sup>14</sup>C Sample Preparation Lab of the Hertelendi Laboratory of Environmental Studies (Debrecen, Hungary). *Radiocarbon* **2013**, *55*, 665–676. [[CrossRef](#)]
38. Molnár, M.; Rinyu, L.; Veres, M.; Seiler, M.; Wacker, L.; Synal, H.-A. EnvironMICADAS: A Mini <sup>14</sup>C AMS with Enhanced Gas Ion Source Interface in the Hertelendi Laboratory of Environmental Studies (HEKAL), Hungary. *Radiocarbon* **2013**, *55*, 338–344. [[CrossRef](#)]
39. Synal, H.-A.; Stocker, M.; Suter, M. MICADAS: A New Compact Radiocarbon AMS System. *Nucl. Instrum. Methods Phys. Res. Sect. B Beam Interact. Mater. At.* **2007**, *259*, 7–13. [[CrossRef](#)]
40. Wacker, L.; Bonani, G.; Friedrich, M.; Hajdas, I.; Kromer, B.; Němec, M.; Ruff, M.; Suter, M.; Synal, H.-A.; Vockenhuber, C. MICADAS: Routine and High-Precision Radiocarbon Dating. *Radiocarbon* **2010**, *52*, 252–262. [[CrossRef](#)]
41. Pécsi, M. Loess Is Not Just the Accumulation of Dust. *Quat. Int.* **1990**, *7–8*, 1–21. [[CrossRef](#)]
42. Pye, K. The Nature, Origin and Accumulation of Loess. *Quat. Sci. Rev.* **1995**, *14*, 653–667. [[CrossRef](#)]
43. Blaauw, M. Methods and Code for “Classical” Age-Modelling of Radiocarbon Sequences. *Quat. Geochronol.* **2010**, *5*, 512–518. [[CrossRef](#)]
44. Bennett, K.D. Confidence Intervals for Age Estimates and Deposition Times in Late-Quaternary Sediment Sequences. *The Holocene* **1994**, *4*, 337–348. [[CrossRef](#)]
45. Blaauw, M.; Heegaard, E. Estimation of Age-Depth Relationships. In *Tracking Environmental Change Using Lake Sediments*; Birks, H.J.B., Lotter, A.F., Juggins, S., Smol, J.P., Eds.; Developments in Paleoenvironmental Research; Springer: Dordrecht, The Netherlands, 2012; Volume 5, pp. 379–413, ISBN 978-94-007-2744-1.
46. Blaauw, M.; Christen, J.A. Flexible Paleoclimate Age-Depth Models Using an Autoregressive Gamma Process. *Bayesian Anal.* **2011**, *6*, 457–474. [[CrossRef](#)]
47. Reimer, P.J.; Austin, W.E.N.; Bard, E.; Bayliss, A.; Blackwell, P.G.; Bronk Ramsey, C.; Butzin, M.; Cheng, H.; Edwards, R.L.; Friedrich, M.; et al. The IntCal20 Northern Hemisphere Radiocarbon Age Calibration Curve (0–55 Cal kBP). *Radiocarbon* **2020**, *62*, 725–757. [[CrossRef](#)]
48. Bronk Ramsey, C.; Higham, T.; Leach, P. Towards High-Precision AMS: Progress and Limitations. *Radiocarbon* **2004**, *46*, 17–24. [[CrossRef](#)]
49. Blaauw, M.; Christen, J.A.; Bennett, K.D.; Reimer, P.J. Double the Dates and Go for Bayes—Impacts of Model Choice, Dating Density and Quality on Chronologies. *Quat. Sci. Rev.* **2018**, *188*, 58–66. [[CrossRef](#)]
50. Frechen, M.; Oches, E.; Kohfeld, K. Loess in Europe—Mass Accumulation Rates during the Last Glacial Period. *Quat. Sci. Rev.* **2003**, *22*, 1835–1857. [[CrossRef](#)]

51. Kohfeld, K.; Harrison, S.P. Glacial-Interglacial Changes in Dust Deposition on the Chinese Loess Plateau. *Quat. Sci. Rev.* **2003**, *22*, 1859–1878. [[CrossRef](#)]
52. Nugteren, G.; Vandenberghe, J.; Ko van Huissteden, J.; An, Z. A Quaternary Climate Record Based on Grain Size Analysis from the Luochuan Loess Section on the Central Loess Plateau, China. *Glob. Planet. Chang.* **2004**, *41*, 167–183. [[CrossRef](#)]
53. Konert, M.; Vandenberghe, J. Comparison of Laser Grain Size Analysis with Pipette and Sieve Analysis: A Solution for the Underestimation of the Clay Fraction. *Sedimentology* **1997**, *44*, 523–535. [[CrossRef](#)]
54. Vandenberghe, J.; Mùcher, H.; Roebroeks, W.; Gemke, D. Lithostratigraphy and Palaeoenvironment of the Pleistocene Deposits at Maastricht-Belvédère. *Meded. Rijks Geol. Dienst* **1985**, *39*, 7–18.
55. Vandenberghe, J.; Nugteren, G. Rapid Climatic Changes Recorded in Loess Successions. *Glob. Planet. Chang.* **2001**, *28*, 1–9. [[CrossRef](#)]
56. Vandenberghe, J. Grain Size of Fine-Grained Windblown Sediment: A Powerful Proxy for Process Identification. *Earth-Sci. Rev.* **2013**, *121*, 18–30. [[CrossRef](#)]
57. Rousseau, D.D.; Antoine, P.; Hatté, C.; Lang, A.; Zöller, L.; Fontugne, M.; Othman, D.B.; Luck, J.M.; Moine, O.; Labonne, M.; et al. Abrupt Millennial Climatic Changes from Nussloch (Germany) Upper Weichselian Eolian Records during the Last Glaciation. *Quat. Sci. Rev.* **2002**, *21*, 1577–1582. [[CrossRef](#)]
58. Rousseau, D.; Sima, A.; Antoine, P.; Hatté, C.; Lang, A.; Zöller, L. Link between European and North Atlantic Abrupt Climate Changes over the Last Glaciation. *Geophys. Res. Lett.* **2007**, *34*, 2007GL031716. [[CrossRef](#)]
59. Zhou, L.P.; Oldfield, F.; Wintle, A.G.; Robinson, S.G.; Wang, J.T. Partly Pedogenic Origin of Magnetic Variations in Chinese Loess. *Nature* **1990**, *346*, 737–739. [[CrossRef](#)]
60. An, Z.; Kukla, G.J.; Porter, S.C.; Xiao, J. Magnetic Susceptibility Evidence of Monsoon Variation on the Loess Plateau of Central China during the Last 130,000 Years. *Quat. Res.* **1991**, *36*, 29–36. [[CrossRef](#)]
61. Rousseau, D.-D.; Kukla, G. Late Pleistocene Climate Record in the Eustis Loess Section, Nebraska, Based on Land Snail Assemblages and Magnetic Susceptibility. *Quat. Res.* **1994**, *42*, 176–187. [[CrossRef](#)]
62. Sun, J.; Liu, T. Multiple Origins and Interpretations of the Magnetic Susceptibility Signal in Chinese Wind-Blown Sediments. *Earth Planet. Sci. Lett.* **2000**, *180*, 287–296. [[CrossRef](#)]
63. Zhu, R.; Liu, Q.; Jackson, M.J. Paleoenvironmental Significance of the Magnetic Fabrics in Chinese Loess-Paleosols since the Last Interglacial (<130 Ka). *Earth Planet. Sci. Lett.* **2004**, *221*, 55–69. [[CrossRef](#)]
64. Dearing, J.A.; Hay, K.L.; Baban, S.M.J.; Huddleston, A.S.; Wellington, E.M.H.; Loveland, P.J. Magnetic Susceptibility of Soil: An Evaluation of Conflicting Theories Using a National Data Set. *Geophys. J. Int.* **1996**, *127*, 728–734. [[CrossRef](#)]
65. Walter, E.; Dean, J. Determination of Carbonate and Organic Matter in Calcareous Sediments and Sedimentary Rocks by Loss on Ignition: Comparison With Other Methods. *SEPM J. Sediment. Res.* **1974**, *44*, 242–248. [[CrossRef](#)]
66. Heiri, O.; Lotter, A.F.; Lemcke, G. Loss on Ignition as a Method for Estimating Organic and Carbonate Content in Sediments: Reproducibility and Comparability of Results. *J. Paleolimnol.* **2001**, *25*, 101–110. [[CrossRef](#)]
67. Krolopp, E. A Magyarországi Pleisztocén Képződmények Malakológiai Tagolása. CSc Thesis, Hungarian National Geological Institute, Budapest, Hungary, 1983.
68. Sümegi, P. Az ÉK-Magyarországi Lösszterületek Összehasonlító Őskörnyezeti Rekonstrukciója És Rétegtani Értékelése. CSc Thesis, University of Debrecen, Debrecen, Hungary, 1996.
69. Sümegi, P. A Hajdúság Felső-Pleisztocén Fejlődéstörténete Finomrétegtani (Üledékföldtani, Óslénytani, Geokémiai) Vizsgálatok Alapján. Ph.D. Thesis, University of Debrecen, Debrecen, Hungary, 1989.
70. Krolopp, E.; Sümegi, P. Palaeoecological Reconstruction of the Late Pleistocene, Based on Loess Malacofauna in Hungary. *GeoJournal* **1995**, *36*, 213–222. [[CrossRef](#)]
71. Sümegi, P.; Krolopp, E. A magyarországi würm korú löszök képződésének paleoökológiai rekonstrukciója Mollusca-fauna alapján. *Földt. Közöny* **1995**, *125*, 125–148.
72. Rousseau, D.-D.; Puisségur, J.-J.; Lautridou, J.-P. Biogeography of the Pleistocene Pleniglacial Malacofaunas in Europe. Stratigraphic and Climatic Implications. *Palaeogeogr. Palaeoclim. Palaeoecol.* **1990**, *80*, 7–23. [[CrossRef](#)]
73. Moine, O.; Rousseau, D.; Antoine, P. Terrestrial Molluscan Records of Weichselian Lower to Middle Pleniglacial Climatic Changes from the Nussloch Loess Series (Rhine Valley, Germany): The Impact of Local Factors. *Boreas* **2005**, *34*, 363–380. [[CrossRef](#)]
74. Magurran, A.E. *Ecological Diversity and Its Measurement*; Springer: Dordrecht, The Netherlands, 1988; ISBN 978-94-015-7360-3.
75. Henderson, P.A.; Southwood, R. *Ecological Methods*, 4th ed.; John Wiley & Sons, Inc.: Chichester, UK; Hoboken, NJ, USA, 2016; ISBN 978-1-118-89527-6.
76. Rousseau, D.-D. Statistical Analyses of Loess Molluscs for Paleoecological Reconstructions. *Quat. Int.* **1990**, *7–8*, 81–89. [[CrossRef](#)]
77. Greenacre, M.J. *Theory and Applications of Correspondence Analysis*; Academic Press: London, UK; Orlando, FL, USA, 1984; ISBN 978-0-12-299050-2.
78. Rousseau, D.-D. Paleoclimatology of the Achenheim Series (Middle and Upper Pleistocene, Alsace, France) A. Malacological Analysis. *Palaeogeogr. Palaeoclim. Palaeoecol.* **1987**, *59*, 293–314. [[CrossRef](#)]
79. Podani, J. *Introduction to the Exploration of Multivariate Biological Data*; Backhuys: Leiden, The Netherlands, 2000; ISBN 978-90-5782-067-0.
80. Rousseau, D.-D.; Limondin, N.; Puissegur, J.-J. Holocene Environmental Signals from Mollusk Assemblages in Burgundy (France). *Quat. Res.* **1993**, *40*, 237–253. [[CrossRef](#)]

81. Dowdeswell, J.A. Relative Dating of Late Quaternary Deposits Using Cluster and Discriminant Analysis, Audubon Cirque, Mt. Audubon, Colorado Front Range. *Boreas* **1982**, *11*, 151–161. [[CrossRef](#)]
82. Hammer, Ø.; Harper, D.; Ryan, P. PAST: Paleontological Statistics Software Package for Education and Data Analysis. *Palaeontol. Electron.* **2001**, *4*, 9.
83. Stevens, T.; Marković, S.B.; Zech, M.; Hambach, U.; Sümege, P. Dust Deposition and Climate in the Carpathian Basin over an Independently Dated Last Glacial–Interglacial Cycle. *Quat. Sci. Rev.* **2011**, *30*, 662–681. [[CrossRef](#)]
84. Perić, Z.; Lagerbäck Adolphi, E.; Stevens, T.; Újvári, G.; Zeeden, C.; Buylaert, J.-P.; Marković, S.B.; Hambach, U.; Fischer, P.; Schmidt, C.; et al. Quartz OSL Dating of Late Quaternary Chinese and Serbian Loess: A Cross Eurasian Comparison of Dust Mass Accumulation Rates. *Quat. Int.* **2019**, *502*, 30–44. [[CrossRef](#)]
85. Bond, G.; Broecker, W.; Johnsen, S.; McManus, J.; Labeyrie, L.; Jouzel, J.; Bonani, G. Correlations between Climate Records from North Atlantic Sediments and Greenland Ice. *Nature* **1993**, *365*, 143–147. [[CrossRef](#)]
86. Björck, S.; Walker, M.J.C.; Cwynar, L.C.; Johnsen, S.; Knudsen, K.-L.; Lowe, J.J.; Wohlfarth, B. INTIMATE Members An Event Stratigraphy for the Last Termination in the North Atlantic Region Based on the Greenland Ice-Core Record: A Proposal by the INTIMATE Group. *J. Quat. Sci.* **1998**, *13*, 283–292. [[CrossRef](#)]
87. Maher, B.A. Magnetic Properties of Modern Soils and Quaternary Loessic Paleosols: Paleoclimatic Implications. *Palaeogeogr. Palaeoclim. Palaeoecol.* **1998**, *137*, 25–54. [[CrossRef](#)]
88. Xie, Q.; Chen, T.; Xu, H.; Chen, J.; Ji, J.; Lu, H.; Wang, X. Quantification of the Contribution of Pedogenic Magnetic Minerals to Magnetic Susceptibility of Loess and Paleosols on Chinese Loess Plateau: Paleoclimatic Implications. *J. Geophys. Res. Solid Earth* **2009**, *114*, 2008JB005968. [[CrossRef](#)]
89. Clark, P.U.; Dyke, A.S.; Shakun, J.D.; Carlson, A.E.; Clark, J.; Wohlfarth, B.; Mitrovica, J.X.; Hostetler, S.W.; McCabe, A.M. The Last Glacial Maximum. *Science* **2009**, *325*, 710–714. [[CrossRef](#)] [[PubMed](#)]
90. Rasmussen, S.O.; Bigler, M.; Blockley, S.P.; Blunier, T.; Buchardt, S.L.; Clausen, H.B.; Cvijanovic, I.; Dahl-Jensen, D.; Johnsen, S.J.; Fischer, H.; et al. A Stratigraphic Framework for Abrupt Climatic Changes during the Last Glacial Period Based on Three Synchronized Greenland Ice-Core Records: Refining and Extending the INTIMATE Event Stratigraphy. *Quat. Sci. Rev.* **2014**, *106*, 14–28. [[CrossRef](#)]
91. Hemming, S.R. Heinrich Events: Massive Late Pleistocene Detritus Layers of the North Atlantic and Their Global Climate Imprint. *Rev. Geophys.* **2004**, *42*, 2003RG000128. [[CrossRef](#)]

**Disclaimer/Publisher’s Note:** The statements, opinions and data contained in all publications are solely those of the individual author(s) and contributor(s) and not of MDPI and/or the editor(s). MDPI and/or the editor(s) disclaim responsibility for any injury to people or property resulting from any ideas, methods, instructions or products referred to in the content.